frontiers in Earth Science

ORIGINAL RESEARCH
published: 23 March 2022
doi: 10.3389/feart.2022.849079

Interpretation of Magnetic Anomalies by Simple Geometrical Structures Using the Manta-Ray Foraging Optimization

Ubong C. Ben[1], Stephen E. Ekwok[1], Anthony E. Akpan[1], Charles C. Mbonu[2], Ahmed M. Eldosouky[3], Kamal Abdelrahman[4] and David Gómez-Ortiz[5]*

[1]Department of Geophysics, University of Calabar, Calabar, Nigeria, [2]Department of Physics, University of Uyo, Uyo, Nigeria, [3]Geology Department, Faculty of Science, Suez University, Suez, Egypt, [4]Department of Geology and Geophysics, College of Science, King Saud University, Riyadh, Saudi Arabia, [5]Department of Biology and Geology, Physics and Inorganic Chemistry, ESCET, Universidad Rey Juan Carlos, Móstoles, Spain

In this paper, a geophysical strategy based on the recently proposed Manta-Ray Foraging (MRF) Optimization algorithm is adapted and presented for the blind computation of depth/shape defining parameters from magnetic anomalies due to buried geo-bodies. The model parameters deciphered are the coefficient of amplitude (K), buried structure's origin (x_0), the depth (z), magnetization angle (α), and a shape factor (q). After detailed and piecewise design, the new inversion tool is originally trial-tested on anomaly data generated synthetically. The uncorrupted version of the test data is first analyzed, then - it is corrupted with noise varied at 5, 10, 15, and 20% corruption levels. Thereafter, it is experimented with magnetic profiles taken from exploration fields in the United States, Peru, and Egypt. From the evaluation of results obtained, the new procedure is observed as exhibiting outstanding stability and flexibility especially with noisy dataset and notable efficiency in the quantitative resolution of magnetic inversion problems. The results obtained for the field cases are also mostly consistent especially when compared with background results from similar studies conducted with other methods; further affirming the new tool as reliable for the geophysical investigation of buried minerals.

Keywords: shapes, anomaly, optimization, manta ray minerals, interpretation, magnetics

OPEN ACCESS

Edited by:
Mourad Bezzeghoud, Universidade de Évora, Portugal

Reviewed by:
Khalid ESSA, Cairo University, Egypt
Arkoprovo Biswas, Banaras Hindu University, India
Salah Mehanee, Cairo University, Egypt

****Correspondence:***
Ahmed M. Eldosouky
dr_a.eldosoky@yahoo.com

Specialty section:
This article was submitted to Solid Earth Geophysics, a section of the journal Frontiers in Earth Science

Received: *05 January 2022*
Accepted: *28 February 2022*
Published: *23 March 2022*

Citation:
Ben UC, Ekwok SE, Akpan AE, Mbonu CC, Eldosouky AM, Abdelrahman K and Gómez-Ortiz D (2022) Interpretation of Magnetic Anomalies by Simple Geometrical Structures Using the Manta-Ray Foraging Optimization. Front. Earth Sci. 10:849079. doi: 10.3389/feart.2022.849079

INTRODUCTION

Magnetic, gravity, electromagnetic, DC resistivity and self-potential techniques have successful applications in mineral exploration (e.g., Biswas et al., 2014; Portniaguine & Zhdanov, 2000a; Mehanee & Zhdanov, 2004; Pellerin & Wannamaker, 2005; Essa et al., 2021; Mehanee, 2022a; Mehanee, 2022b). Synonymous with other conventional geophysical methods, optimal interpretations require that magnetic field data be analyzed in ways generally deemed best for the recovery of characteristic parameters mirroring those of the features causing the anomalies (Klein et al., 2016; Balkaya et al., 2017; Xie et al., 2019; Ben et al., 2021c). Generally, geologic structures are extensively classified into four geometrical categories: spheres, thin sheets, infinitely long cylinders, and geological contacts (Ben et al., 2021a). These simple geometric models conveniently approximate structures that are commonly in during magnetic data interpretation. Geophysical inversion aims at unraveling parameters characteristic of geologic structures through numerical adjustments to these

already defined models (Essa & Elhussein, 2020; Essa et al., 2020). The notably sought-for parameters are usually those defining anomaly position (in space), depth, and those characterizing the anomaly shape (Ekinci et al., 2021; Essa et al., 2021; Mehanee, 2022b).

A review of published literature reveals that several strategies have been priorly employed for magnetic inversion. An adept number of them take advantage of computational approaches such as those consistent with classical/numerical theories. Gay (1965) using conventional curve fitting theories developed standard curves for common geologic structures. Abo-Ezz & Essa (2016) introduced a linear least-squares method for the deciphering of buried geologic bodies from magnetic anomaly profiles. Araffa et al. (2018) employed Euler deconvolution to delineate subsurface structural features of basement complex from magnetic data. Ouyang & Chen (2020) iteratively modeled magnetic anomalies using the Fourier transform technique. Duong et al. (2021) interpreted magnetic data at low latitude areas using Marquardt algorithm and continuous wavelet transform. Some of other deterministic methods experimented and reported in literature for magnetic anomalies include fair function minimization procedures (Asfahani & Tlas, 2012; Abbas & Fedi, 2013), simplex algorithm (Pan et al., 2009; Abdelrahman et al., 2019), regularized inversion and image focusing (Portniaguine & Zhdanov, 2000b) and Hilbert Transform (Dondurur and Pamukçu, 2003). However, these inversion techniques sometimes generate poor solutions mostly accrued to causatives such as recursive noise, window size incompatibility and the number of data points considered in the interpretation out of the entire magnetic data profile. Furthermore, the majority of them rely heavily on a series of initializations derived from subjective historical geologic deductions. This pre-knowledge is not always available and even if they are, their reputability can sometimes be disputed.

With recent advancements in machine intelligence and with increased efforts to address the aforementioned challenges, interpretative heuristic methodologies are increasingly being introduced for magnetic anomaly interpretations. Some of these methodologies are based on; genetic algorithm, particle swarm, differential evolution, ant colony optimization, and genetic-price algorithm. Liu et al. (2015) optimized interpretation of surface and subsurface magnetic measurements using ant colony optimization. Biswas & Acharya (2016) deployed VFSA for the interpretation and modeling of magnetic anomaly over a vertically magnetized rod-like structure. Biswas et al. (2017) developed an approach to the estimation model parameters from the total gradient of magnetic data based on Very Fast simulated Annealing (VFSA). Agarwal et al. (2018) developed a grey-wolf optimer based

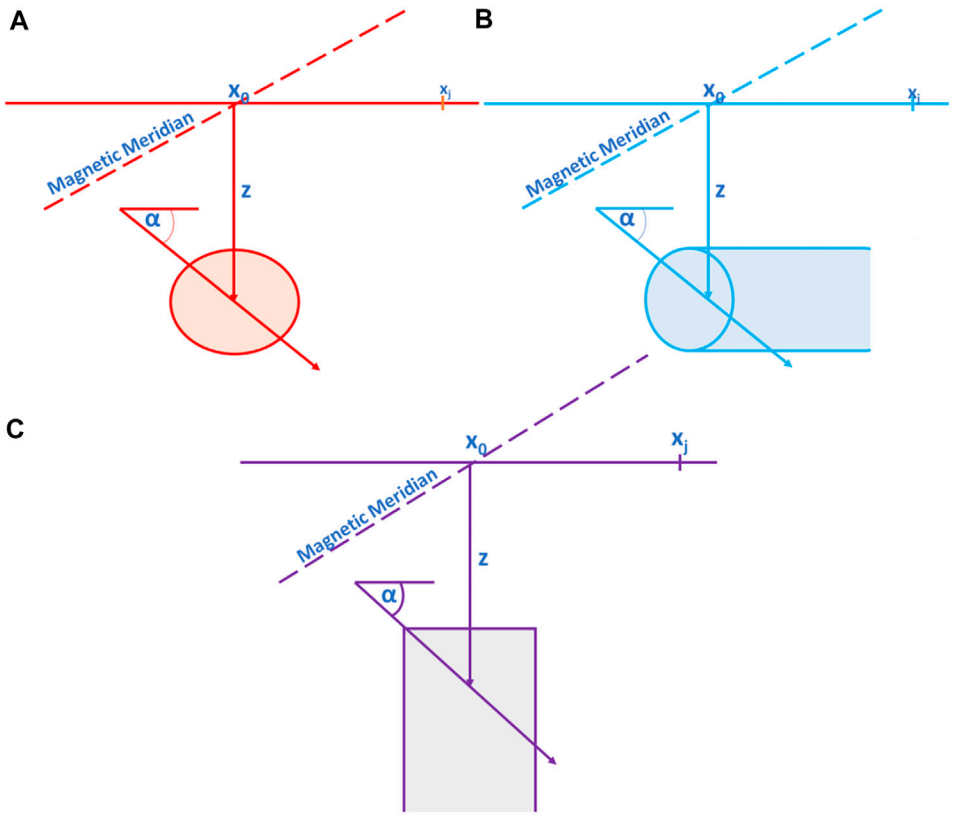

FIGURE 1 | Schematic cross-sections showing configurations of simple geometrical shaped models and their parameters; **(A)** Sphere **(B)** Horizontal cylinder **(C)** Thin sheet.

TABLE 1 | Characteristic inclination parameter for vertical, horizontal and total magnetic field anomalies due to thin sheets and horizontal cylinders (after Gay, 1963, Gay, 1965).

Magnetic Field	Inclination Parameter	
	Thin sheet	Horizontal cylinder
Vertical	I_T-§	I_T-90
Horizontal	I_T-§-90	I_T-180
Total	$2I_T$-§-90	$2I_T$-180

methodology for the inversion of magnetic datasets from surface and airborne surveys. Ekinci et al. (2019) in their comparative study analyzed the performance of differential evolution against particle swarm optimization for magnetic parameterization through direct search. Essa & Elhussein (2020) emphasized the employment of particle swarm optimization for the inferring of residual magnetic anomalies. Di Maio et al. (2020) introduced a hybrid genetic-price heuristic for the inverse modeling of magnetic anomalies due to simple geological structures. Gobashy et al. (2020) introduced the Whale Optimization Algorithm for the assessment of model parameters from magnetic anomalies over mineralization structures. Balkaya & Kaftan (2021) conducted inverse modeling of intrusive structures using differential search algorithm. Essa et al. (2021) applied the variance analysis method for magnetic profile interpretation. Mehanee et al. (2021) carried out magnetic modeling using a R-parameter imaging approach. Balkaya & Kaftan (2021) interpreted magnetic anomalies caused by dyke-shaped bodies using differential search algorithm. Du et al. (2021) proposed a new method to conduct lp norm magnetic inversion of 2D data using adaptive differential evolution technique. The most obvious advantage of meta-heuristics techniques is that unlike their analytical strategies, improvements in directions referencing the feasible solution are not influenced by the gradients of the minimized objective function (Kombe & Muguthu, 2019; Elaziz et al., 2020; Hayyolalam & Pourhaji Kazem, 2020).

Noting the meritoriousness of the aforementioned, especially in interpretative resolvability of buried structures, the reader may be puzzled as to why a new optimizer-based procedure is still developed to solve problems that previous optimizers have already solved. A geophysical interpretation of the infamous No Free Lunch Theorem of Optimization (Salcedo-Sanz et al., 2018; Gharehchopogh & Gholizadeh, 2019; Gupta & Deep, 2019) presents an appropriate response to this question. This is that, while the majority of the previously proposed methodologies based on intelligent optimization algorithms have greatly improved anomaly interpretation quality, analytical perfection has yet to be achieved, particularly in terms of convergence and computation complexity. The continuous pursuit of analytical perfection necessitates the testing of new optimizers. This is also the primary motivation for this research. In this research paper, we present a new interpretative methodology for describing geophysical anomalies over different geometrically-shaped geologic bodies. The methodology is based on the manta-ray foraging (MRF) optimization algorithm.

The MRF algorithm–originally introduced by Zhao et al. (2020) leverages the foraging actions of manta rays for resolving physical optimization problems. This is accomplished by imitating the chain, cyclone, and saumasault foraging techniques–three of the manta ray's most efficient foraging strategies. Ensuing experimentations in other fields such as pharmacy and engineering, the optimization technique was found to outperform existing metaheuristic algorithms especially in the aspects of computing cost, performance, and solution accuracy (Elaziz et al., 2020; Hemeida et al., 2020; Xu et al., 2020; Ghosh et al., 2021; Hassan et al., 2021; Houssein et al., 2021), the method has been recommended for the resolution of structural problems such as those in geophysics (Elaziz et al., 2020; Xu et al., 2020; Ghosh et al., 2021; Houssein et al., 2021). It is worthy to note the efforts of Ben et al. (2021b) with vertically dipping dykes and Ben et al. (2021a) with gravity anomalies. Howbeit, to the best of the authors' knowledge, and at the time of preparation of the initial drafting of this research paper, no study in published literature has explicitly employed MRF algorithm for the modeling of magnetized subsurface materials of geometric structure. The new method presents a couple of merits. First, unlike deterministic schemes, iterative computations are independent of the gradient of the objective function, technically limiting immature convergence. Also, the wild function injected during the cyclone foraging stage of the algorithm design allows initial models to parametrize from anywhere within a size-independent range (as would be seen in the examples)—reducing reliance on subjectivity. Most importantly, the superiority of the MRF tool actually lies with its foraging character. With MRF algorithm, the search agents are allowed to switch intelligently and at any point between the strategies of chain foraging and cyclone foraging. The chain foraging behavior allows significant local search while the

TABLE 2 | Definitions of A, B and C parameters.

Parameter	Sphere (total mag. Field)	Sphere (vertical mag. Field)	Spheres (horizontal mag. Field)	Horizontal cylinders; thin sheets (FHD); geological contacts (SHD), (all fields)	Thin sheets; geological contacts (FHD) (all fields)
A	$3\sin^2\alpha - 1$	$2\sin\alpha$	$-\cos\alpha$	$\cos\alpha$	$\frac{\cos\alpha}{z}$
B	$-3z\sin(2\alpha)$	$-3z\cos\alpha$	$-3z\sin\alpha$	$2z\sin\alpha$	$\sin\alpha$
C	$3\cos^2\alpha - 1$	$-\sin\alpha$	$2\cos\alpha$	$-\cos\alpha$	0

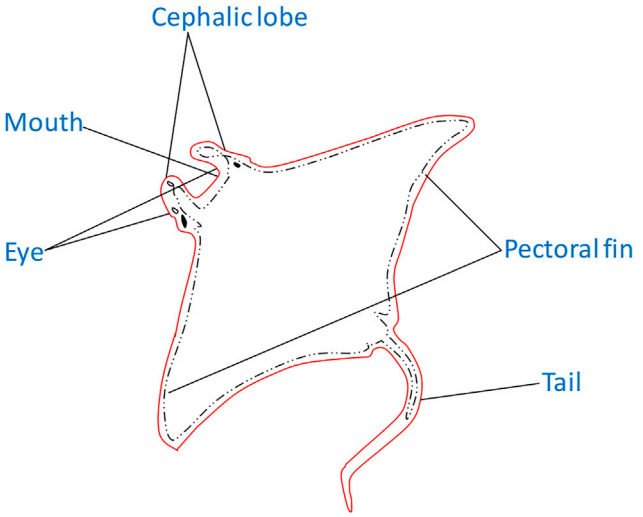

FIGURE 2 | Anatomical structure of a conventional Manta ray.

cyclone foraging behavior concurrently assures non-deteororation of global search during the process; a mutualization of the two as allowed by the new technique ensures comparatively quality solutions through thorough exploration of the whole domain of the geophysical problem.

The paper begins with a magnetic inversion problem layout and a step-by-step architecture of the MRF-based inversion technique. The approach is then trial-tested through applications to synthetic models that have been contaminated with varying degrees of Gaussian random noise (0, 5, 10, 20, and 20%) as well as anomalies from multiple/interfering models. The methodology's performance with real-world anomalies is gauged using field profiles taken from geologically-contrast exploration mining areas. The resultant parameter values are then compared against drilling results and those obtained using other traditional approaches and documented in literature. Finally, we conclude the paper with a review of the adaptability and performance of MRF optimization method as an inversion tool for magnetic anomalies as well as its gains and limitations with respect to previous techniques.

Initialize population, T and individual manta rays $y^4_i(t) = y^4_i + rand().(LB-UB)$ for i=1,2,...,N and t=1
Calculate fitness for each individual and obtain y^4_{best}
while stopping criterion is not satisfied? **do**
  for i = 1,2,3,....N do
    if rand() < 0.5 then #*Cyclone Foraging*
      if t/T < rand() **then**
        $y^4_i(t+1) = \begin{cases} y^4_{best}(t) + rand().(y^4_{best}(t) - y^4_i(t)) + \mu.(y^4_{best}(t) - y^4_i(t)) & i=1 \\ y^4_{best}(t) + rand().(y^4_{i-1}(t) - y^4_i(t)) + \mu.(y^4_{best}(t) - y^4_i(t)) & i=2,3,\ldots,T \end{cases}$
      else
    else #*Chain Foraging*
      $y^4_i(t+1) = \begin{cases} y^4_i(t) + r.(y^4_{best}(t) - y^4_i(t)) + w.(y^4_{best}(t) - y^4_i(t)) & i=1 \\ y^4_i(t) + r.(y^4_{i-1}(t) - y^4_i(t)) + w.(y^4_{best}(t) - y^4_i(t)) & i=2,3,\ldots,T \end{cases}$
      end if
    Calcute fitness for *ith* individual $f(y^4_i(t+1))$
    if $f(y^4_i(t+1)) < f(y^4_{best})$ **then**
      $y^4_{best} = y^4_i(t+1)$
    end if
  end for
  #*Somersault Foraging*
  for i = 1...N **do**
    $y^4_i(t+1) = y^4_i(t) + P.(rand_1().y^4_i(t) - rand_2().y^4_i(t), \quad i = 1, 2, \ldots, N$
  Calculate fitness for ith individual $f(y_i(t+1))$
    if $f(y^4_i(t+1)) < f(y^4_{best})$ **then**
      $y^4_{best} = y_i(t+1)$
    end if
  end for
end while
return y^4_{best}

FIGURE 3 | Pseudocode of the MRF algorithm.

TABLE 3 | Estimated parameters for the example involving synthetically generated noise-free models.

Type of model	Parameters	True	Estimated				
			Noise free	5% noise	10% noise	15% noise	20% noise
Sphere	K (nT.m^3)	11000.000	11001.300	11615.407	11907.531	12006.877	12294.040
	α (^{0})	60.000	60.000	60.983	61.217	59.745	60.022
	z (m)	11.000	11.000	11.629	11.892	12.105	12.205
	x_0(m)	0.000	0.000	0.001	0.001	0.000	0.000
	q	2.500	2.500	2.503	2.498	2.502	2.492
	Time elapsed		31s	33s	35s	35s	37s
Horizontal Cylinder	K (nT.m^2)	400.000	401.021	402.573	387.476	376.085	421.741
	α (^{0})	35.000	34.998	34.861	33.904	31.653	30.002
	z (m)	5.000	5.000	5.388	5.142	5.271	5.300
	x_0(m)	0.000	0.000	0.000	0.002	- 0.007	0.003
	q	2.000	2.000	2.000	1.986	2.002	2.007
	Time elapsed		30s	32s	32s	34s	36s
Thin Sheet	K (nT.m)	550.000	550.000	550.041	545.703	543.681	558.039
	α (0)	30.000	30.000	30.584	29.628	28.518	29.711
	z (m)	9.000	9.000	8.927	8.887	8.700	8.768
	x_0(m)	0.00	0.002	0.004	0.010	0.012	0.016
	q	1.00	1.005	1.002	1.005	1.009	1.015
	Time Elapsed		32s	34s	35s	37s	40s

METHODOLOGY

Geophysical Inversion and the Magnetic Anomaly Problem

In geophysical exploration, magnetic data inversion is generally initiated by transforming so-called ill-posed problems to optimization models constructed such that the parameters of the model explained by observation data are good descriptions of the subsurface anomaly (Mehanee et al., 1998; Liu et al., 2015; Essa & Elhussein, 2020; Mbonu et al., 2021). The process of finding a solution to an inverse problem normally begins with the supposition of a good initial model. This initial model commonly made from drilling data or reports from previous geophysical expositions is progressively smoothened in stepwise iterative runs until a subjectively suitable fit between the measured and estimated data is acquired. The smoothening is executed by making meta-heuristic forward adjustments to the parameters of the model (Gharehchopogh & Gholizadeh, 2019; Wang & Li, 2019; Hayyolalam & Pourhaji Kazem, 2020). In this research, the model parameters of interest are amplitude coefficient (K) related to the composition of the body, depth (z), location of the origin (x_o), angle of magnetization (α), and a shape factor (q) whose value is unique for each different structural shape (**Figure 1**)

For this study, we employ the general formula for magnetic anomaly profile -T (x_j) over simple-geometrically shaped structures meticulously extrapolated from the inductive analysis of mathematical expressions for horizontal, vertical, and total magnetic anomaly of spheres (Prakasa Rao & Subrahmanyam, 1988), horizontal cylinders (Rao et al., 1973) and thin sheets (Gay, 1963). The formula (**Equation 1**) is given as (Mehanee et al., 2021):

$$T(x_j) = K\frac{Az^2 + B(x_j - x_0) + C(x_j - x_0)^2}{\left[(x_j - x_0)^2 + z^2\right]^q},\ j = 1, 2, 3, 4, \ldots \quad (1)$$

where z is depth to the buried anomaly, K the amplitude coefficient and, α the angle of magnetization normally in the plane of the principle profile coinciding with the *x*-direction. This is illustrated by Prakasa Rao and Subrahmanyam, 1988) for spheres and compiled by Gay (1965) for horizontal cylinders and thin sheets (**Table 1**). x_0 indicates the coordinate of the center of the structure, §-the dip, I_T the effective inclination of the geomagnetic field in the vertical plane normal to the body's strike while q is the shape factor taken as 2.5 for spheres, 2.0 for infinitely-long horizontal cylinders, and 1.0 for thin geologic sheets (Mehanee et al., 2021). FHD and SHD are the first and second derivatives of the anomaly respectively while A, B, and C constants are defined in **Table 2**;

The five controlling model parameters (K, z, *α*, xo, and q) are computationally obtained by strategically introducing procedures outlined in the succeeding section on the objective function expressed in **Equation 2** (Essa & Elhussein, 2020). Puzzling of optimal parameters for the geophysical model of interest is carried out such that the misfit between the true and estimated data (calculated using the objective function - **Equation 2**) is minimized (Mehanee et al., 1998; Ouadfel & Taleb-Ahmed, 2016).

$$\frac{\sum_{i=1}^{S}\left(T_i^m - T_i^c\right)^2}{S} \quad (2)$$

where T_i^m and T_i^c are respectively the magnetic anomaly from observed data and that estimated using the proposed methodology.

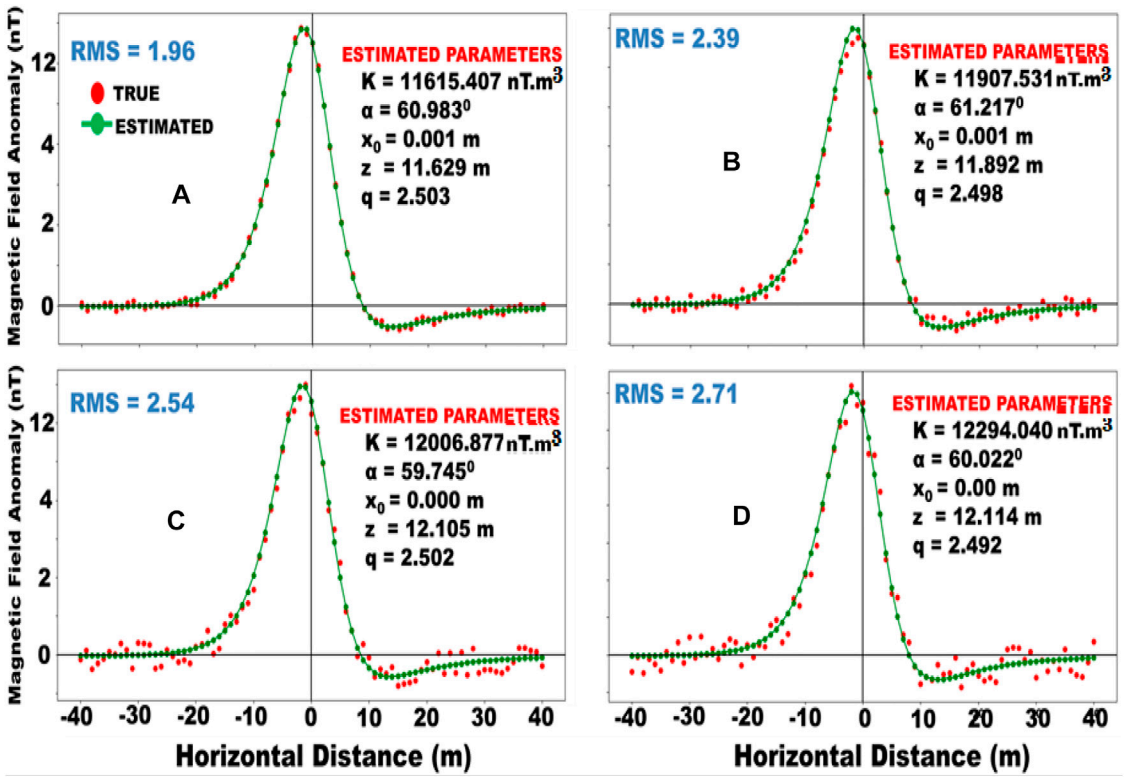

FIGURE 4 | Synthetically generated noisy and estimated (MFR) magnetic anomalies for a sphere model with K = 11,000 nT.m3, z = 11 m, q = 2.5, α = 600, xo = 0 m with **(A)** 5% **(B)** 10% **(C)** 15% **(D)** 20% gaussian random error.

Manta Ray Foraging Optimization Algorithm

The MRF optimization algorithm (which is the backbone of our new methodology) is designed based on the foraging strategies of marine-living Manta rays (**Figure 2**). The foraging strategies include chain, cyclone, and somersault techniques (Ghosh et al., 2021). For our geophysical case, the iterating vectoral positions of the Manta-rays (search agents) represents the probable positions of physical parameters sought-for. The position of the plankton itself (also vectoral) points to the geoscientific optimization problem's solution. For the chain foraging strategy, the agents identify and frame a head-tail formation (also referred to as foraging chain) towards a potential plankton. As a result, any plankton lost by one Manta-ray will not escape the next; thereby improving the overall rate of exploitation. In the cyclone style of foraging, the manta rays swim towards the food in design spirals such that while maintaining its foraging chain-line, each agent is concurrently advancing towards its target food. Alternatively, the solution to the magnetic problem is placed as a pivot in the summersault foraging technique; such that the agents recurrently translate about this pivot before moving into new positions. The result of this is that the new positions are not purely random but rather, circumvents of the best position found (at least up to that point). These numerical constructs for these foraging strategies as adapted from Zhao et al. (2020) and remodeled for our geophysical case are described below; Chain foraging: **Equation 3**

$$T\left(x_j\right)_i^D = \begin{cases} T\left(x_j\right)_i^D(t) + r.\left(T\left(x_j\right)_{best}^D(t) - T\left(x_j\right)_i^D(t)\right) + w.\left(T\left(x_j\right)_{best}^D(t) - T\left(x_j\right)_i^D(t)\right) & i=1 \\ T\left(x_j\right)_i^D(t) + r.\left(T\left(x_j\right)_{i-1}^D(t) - T\left(x_j\right)_i^D(t)\right) + w.\left(T\left(x_j\right)_{best}^D(t) - T\left(x_j\right)_i^D(t)\right) & i=2,3,\ldots,N \end{cases} \quad (3)$$

$$\boldsymbol{w = 2.rand}().\sqrt{|\log(\boldsymbol{r})|} \quad (4)$$

where $T\left(x_j\right)(t)$ is the *i*th search agent's position at a time t. *rand*() –a vector randomly generated within 0 and 1; w- the coefficient of weight, N is the maximum iterations allowed; while $T\left(x_j\right)_{best}^D(t)$ points to the healthiest pool of planktons representing the optimum vectoral position of the sought geomagnetic parameters. The exponentiation factor D represents the dimension of the position. For the study, D = 4 since we are dealing with four parameters **Equation 4**.

Cyclone foraging:

$$T\left(x_j\right)_i^D(t+1) = \begin{cases} T\left(x_j\right)_{best}^D(t) + rand().\left(T\left(x_j\right)_{best}^D(t) - T\left(x_j\right)_i^D(t)\right) + \mu.\left(T\left(x_j\right)_{best}^D(t) - T\left(x_j\right)_i^D(t)\right) & i=1 \\ T\left(x_j\right)_{best}^D(t) + rand().\left(T\left(x_j\right)_{i-1}^D(t) - T\left(x_j\right)_i^D(t)\right) + \mu.\left(T\left(x_j\right)_{best}^D(t) - T\left(x_j\right)_i^D(t)\right) & i=2,3,\ldots,N \end{cases} \quad (5)$$

where μ, known as the cyclone foraging's coefficient of weight, is generated stochastically using **Equation 6**;

$$\boldsymbol{\mu = 2e^{rand()\frac{T-t+1}{T()}}.\sin 2\pi rand}() \quad (6)$$

It is noteworthy to add that after executing **Equation 5** for our structural problem, we uncomfortably observe that the optimizing parameters for our geophysical structure tend to vacillate around a certain position in a loose loop-like manner. To resolve this particularity, we force each of our agents to find new positions far from its current best position in the search space by randomly injecting a wild function q^D_{rand} with the whole search taken as the reference position (Ben et al., 2021b). q^D_{rand} was constructed numerically using **Equation 7**.

$$q^D_{rand} = LB^D + rand().\ (UB^D - LB^D) \tag{7}$$

as such, **Equation 7** became;

$$T(x_j)^D_i(t+1) = \begin{cases} q^D_{rand}(t) + rand().q^D_{rand}(t) - T(x_j)^D_i(t)) + \mu\ .\ (q^D_{rand}(t) - T(x_j)^D_i(t)) & i=1 \\ q^D_{rand}(t) + rand().\ (T(x_j)^D_{i-1}(t) - T(x_j)^D_i(t)) + \mu\ .\ (q^D_{rand}(t) - T(x_j)^D_i(t)) & i=2,3,\ldots,N \end{cases} \tag{8}$$

This strategy that the algorithm extensively performs global search; substantially improving general exploration. **Equation 8**.

Summersault foraging:

$$T(x_j)^D_i(t+1) = T(x_j)(t) + P.\ (rand().T(x_j)^D_i(t) - rand().T(x_j)^D_i(t)),\quad i = 1, 2, \ldots, N \tag{9}$$

where the term P - a constant known as the somersault factor determines the range at which the Manta rays somersault. **Equation 9**.

Generally, the chain strategy encourages individual positioning based on short-term historical positioning and current global best. The cyclone foraging strategy makes each individual update its position with respect to both its preceding neighbor and the reference position while the summersault foraging technique enforces thorough adaptive search.

For exhaustive details about the adoption of the MRF algorithm for optimization scenarios, the readers are referred to Zhao et al. (2020). In our new method, we start by initiating a random population of Manta-rays in the search domain (designed around the upper bound (UB) and lower bound (LB) of our magnetic model parameters) with each agent position in the space representing characteristic parameters of the geologic structure. In our geophysical case, the selection of bounds are done based on priori geological knowledge such as information from maps, geophysical data and drilling reports. At each iterative step, the individuals are coerced to update these positions based on the referential position and the individual out front. This reference position depends on t/T which decreases from 1/T to 1 (Xu et al., 2020; Mbonu & Ben, 2021). With t/T less than rand (), exploitation is implemented else, exploration is performed. Based on this, our MRF optimization algorithm allows the individuals to decide and when necessary, switch between chain and cyclone foraging behaviors. Then through somersault foraging, the agents adaptively update their positions within the space and with respect to the most optimal position so far found.

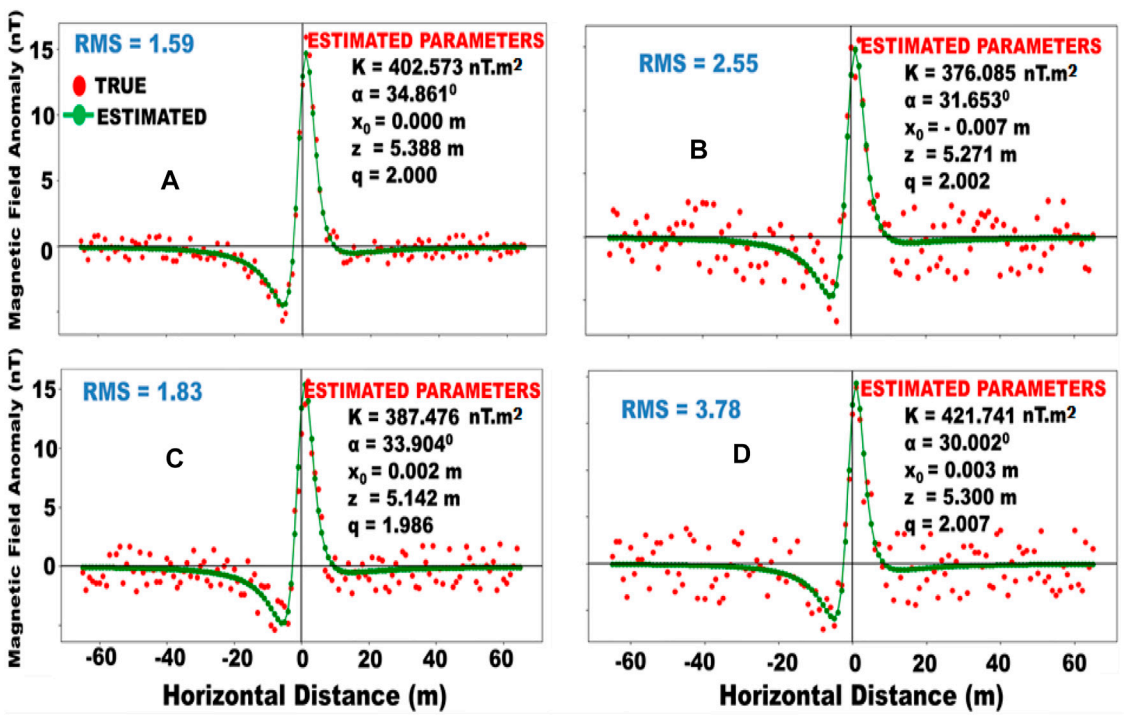

FIGURE 5 | Synthetically generated noisy and estimated (MFR) magnetic anomalies for a horizontal cylinder model with K = 400 nT.m2, z = 5 m, α = 35, q = 2, xo = 0 m, with **(A)** 5% **(B)** 10% **(C)** 15% **(D)** 20% gaussian random error.

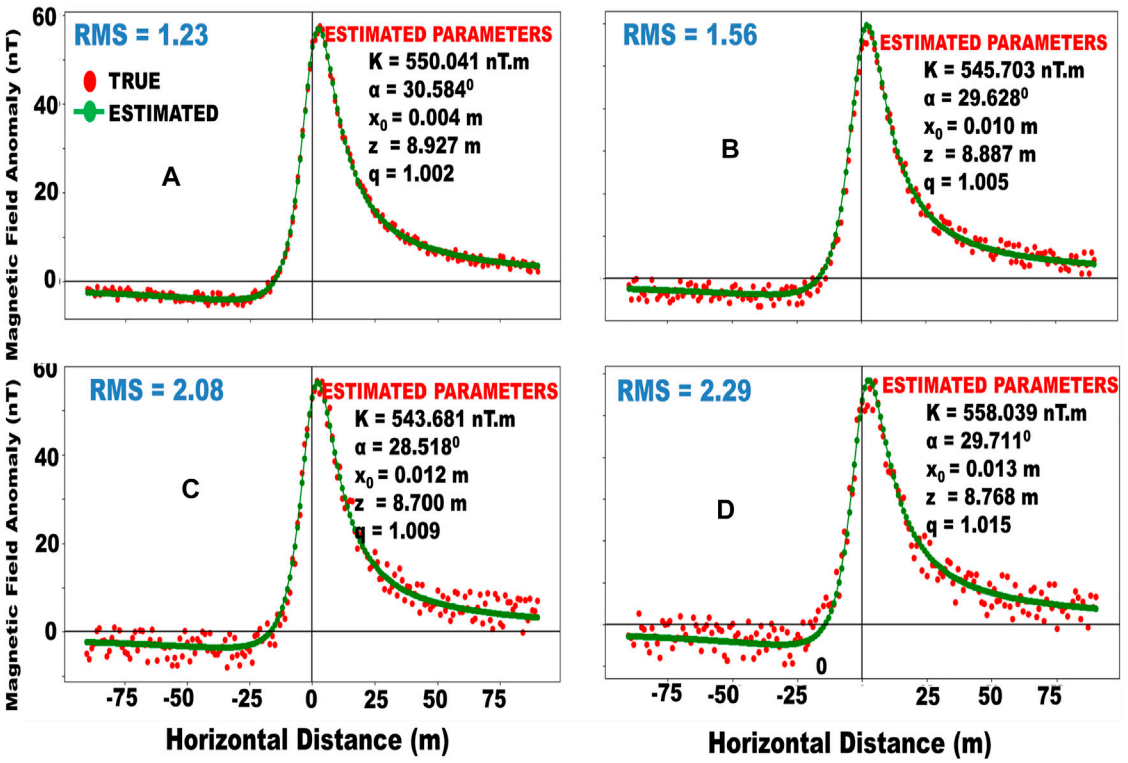

FIGURE 6 | Synthetically generated noisy and estimated (MFR) magnetic anomalies for a thin sheet model with K = 550 nT m, z = 9 m, α = 30, q = 1, xo = 0 m, with **(A)** 5% **(B)** 10% **(C)** 15% **(D)** 20% gaussian random error.

It is noteworthy to add that these calculations and updates explained are interactively performed step-wise until the stopping criterion is met. After each step, the quality is assessed. This is done by gauging the misfit between the measured and estimated anomalies. The misfit is calculated using the root mean technique (Abdelrahman et al., 2012; Mehanee, 2014).

Eventually, convergence is achieved and the four required model parameters are returned. The pseudo-code for the whole optimization process is shown in **Figure 3**.

Algorithm Configuration/Processing Time

The algorithm for this study is designed using the PYTHON programming language and implemented on the virtual studio code IDLE. The IDLE is installed on a PC operating with a Windows 10 operating system and a core i7 processor. The duration of the compilation process is found to depend on the complexity of the anomaly. For simple structures, the iteration process rounds off in 30–50 s. However, there was a 20% increase in processing time for multi-model cases such as those in *Conclusion* Section and Section 5.3. Howbeit, in all cases, the process is found to completely round off in less than 100 s.

RESULTS AND DISCUSSION

The goal of this study is to assess the effectiveness of the MRF optimization technique in modelling magnetic anomalies over geometric geological structures. To monitor this performance, the tool is tested on synthetic and then on field magnetic data.

Synthetic Examples

The proposed method is subjected to controlled experiments using data generated synthetically for idealized spheres, horizontal cylinders, and thin sheet models. First, analysis is done on the synthetic anomaly constructed such that it is noise-free; then the data is consciously corrupted with different levels of noise and reanalyzed.

Noise-Free Models

The MFRO technique is employed to noise-free synthetic anomalies due to geometric interpretative models consisting of: a sphere with K = 11,000 nT m^3, z = 11 m, q = 2.5, α = 60°, x_o = 0 m, and profile length = 80 m; a horizontal cylinder with K = 400 nT m^2, z = 5 m, α = 35, q = 2, x_o = 0 m, and profile length = 120 m, and a thin sheet with K = 550 nT m, z = 9 m, α = 30, q = 1, x_o = 0 m, and profile length = 180 m. The magnetic field anomalies due to these models are computed using **Equation 1**.

The proposed methodology is initiated with 80 initial models and broad search space. For the sphere, we set the range for K to be from 5,000 to 300,000 nT m^3, z from 3 to 15 m, α from -90° to 90°, q from 0 to 3, and x_o from−30 to 30 m. For the horizontal cylinder model, we set K from 100 to 9,000 nT m^2, z from 3 to 15 m, α from -90° to 90°, q from 0 to 3, and x_o from−30 to 30 m. For the thin sheet model, we set K from 100 to 20,000 nT m, z

from 0 to 30 m, α from -90° to 90°, q from 0 to 3, and x_o from−30 to 30 m. A total of 800 repetitive iterations are allowed for each algorithm run. MFRO has very extensive and strong search ability. Impressively, the best model parameters are arrived at in under a quarter of that number of iterations.

From the result obtained (**Table 3**), it is observed that the output for each of the five considered parameters (K, z, α, q, x_o) agree with those originally used to design the three models (with very negligible errors).

Noisy Models

It is well recognized that geophysical data from real buried anomalies are scarcely (if ever) pure. More also, due to the heterogeneity of the earth, it is often very difficult to understand what degree of noise is muddled up in such data. Hence, to delineate the method's efficiency, all the synthetic test data were tweaked to simulate non-ideal geologic scenarios. For this research, the non-ideal geologic scenarios are simulated by contaminating the error-free synthetic anomalies with 5, 10, 15 and 20% white gaussian noise. The noise is generated using a combination of the rand () function and the *SCIPY* library in PYTHON. The noise percentage are computed using **Equation 10** (Mehanee, 2022b).

$$Percentage\ of\ Noise = \frac{||T_n - T||}{||T_n||} \text{x}100 \tag{10}$$

where T_n and T are vectors of the noisy and noise-free anomaly data respectively.

The proposed methodology is once again employed for the estimation of the model-describing parameters. For this, **Equation 2** is re-adopted as the cost function and bounds consistent with the noiseless cases are re-selected. After each iteration session, the convergence and level of misfit are meticulously analyzed.

At the end of the optimization process, it is observed that the algorithm estimates (**Table 3**; **Figures 4–6**) and the true parameter values are to an appreciable level, consistent. However, it is noticed from the results in **Table 3** that the M parameter tends to exhibit more sensitivity with increasing levels of noise. This sensitivity - which would only have likelihood of affecting interpretation when dealing with extremely complicated and deep-seated surface structures is not unrelated to the fact the K is a multiplier factor in **Equation 2**; it can easily be handled by flexibly narrowing ranges for UB and LB. Also, results indicate the misfit after acceptable convergence and the RMS error at the end of the run as marginally upsurging with increasing levels of noise. Nevertheless, this does not wholly affect the general inversion process as parameter results consistently remain attractive even to 20% noise level (**Table 3**). It can thus be concluded that the new methodology is inherently stable and exhibits admirable adeptness in handling noisy anomalies.

Figures 4–6 are plots illustrating the performance of the new technique with synthetic data generated for the three geometric models.

Applicability in Multi-Model Cases

We now seek to assess the new procedure's performance with anomalies from complicated and interfering subsurface structures. To simulate this scenario, we once again generate model data synthetically but, in this scenario, from multiple source bodies (with multifarious parameters) placed at proximity. For the sake of this example, we adopt a horizontal cylinder model with K = 55,000 nT m^2, z = 15 m, α = 25, q = 2, x_o = 30 m, and a thin sheet model with K = 75 nT m, z = 9 m, α = -15, q = 2, x_o = 120 m. The profile length is 400 m. The magnetic field anomaly generated is as shown in **Figure 7**.

We then apply steps consistent with the proposed methodology (as with those in the two preceding sections). However, in this case, the structures are modeled together with parameter bounds as displayed in **Table 4** selected. From results (**Figure 7**; **Table 4**), the parameters can be observed as being well recuperated from and showing admirable consistency with the actual field anomaly confirming the congruency of the methodology.

Comparative Analysis of MRF Optimization With Other Inversion Techniques

In this section, we compare the optimization performance of MRF with those from other methods commonly used for geophysical inversion. In our analysis, we are concerned with the convergence rate, quality/depth of exploration, and accuracy.

For the analysis, three common inversion techniques were selected namely; PSO, SA, and GA.

Particle Swarm Optimization

PSO originally introduced by Kennedy & Eberhart (1995) mimics the behavior of swarms in nature. These swarms may be fish schools or bird flocks. Members of the swarms represent exploring search agents. The technique achieves optimization by updating the positions and velocities of the swarm members based on the positions and velocities of their in-swarm neighbors their movement history. These updates are made using **Equations 11**, **12**;

$$v_i(t+1) = \omega v_i(t) + c_1 r_1 \left(p_i - xi(t)\right) + c_2 r_2 \left(p_g - x_i(t)\right) \tag{11}$$

$$x_i(t+1) = x_i(t) + v_i(t+1) \tag{12}$$

where ω is the inertia constant, c_1 and c_2 are respectively cognitive and social coefficients, pi is the personal optimum of xi, and pg is the global best. For this study, values of 0.729, 2.041, 0.948 were assigned for the inertia weight (ω) and the cognitive and social coefficients.

Simulated Annealing

SA is an optimization procedure the mimics the cooling of metals. The value for the cost function corresponds to energy levels in a melted metal while model parameters are depicted by its molecules' position. For any given parameter set with error ε_0, a new set is methodically generated using random walk. If $\varepsilon < \varepsilon_0$, the new set is discarded, and another is generated. Alternatively, if $\varepsilon \geq \varepsilon_0$, then the set is accepted with a probability defined by Boltzmann's distribution (**Equation 13**):

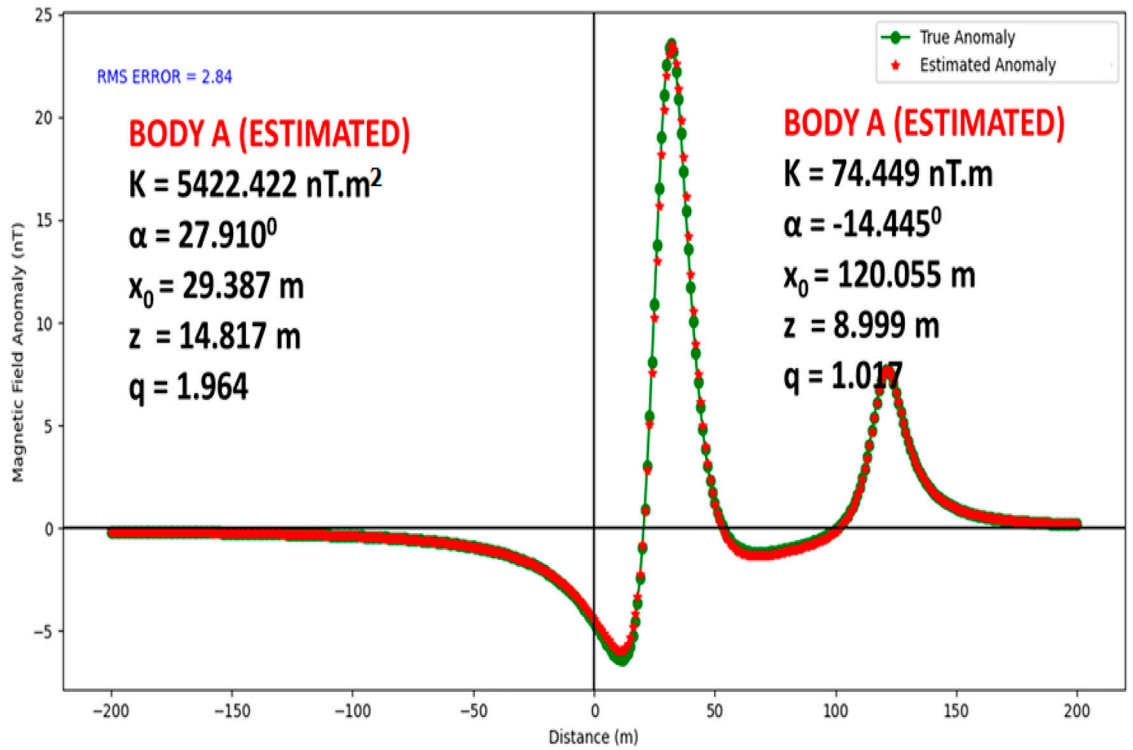

FIGURE 7 | Synthetic and predicted magnetic anomalies of multimodel example consisting of a cylinder model K = 55,000 nT.m2, z = 15 m, α = 25, q = 2.0, xo = 30 m, and a thin sheet model with K = 75 nT m, z = 9 m, α = -15, q = 2, xo = 120 m.

$$f(\Delta E) = e^{\frac{-\Delta\varepsilon}{kT}} \tag{13}$$

where $\Delta\varepsilon = \varepsilon - \varepsilon_0$, T is the temperature while k is the Boltzmann constant. This step is repeated iteratively until an equilibrium state is arrived at. This is a penultimate state where the new set possesses minimum energy at fixed temperature. A generalization of the strategy introduced by Kirkpatrick et al. (1983) adopts a controlled cooling scheme (annealing) where the temperature is gradually (but strategically) reduced with minimum error gauged at each temperature until it arrives at a global minima. For this comparative study, the temperature was reduced by multiplying the previous value by a coefficient less than unity (0.85).

TABLE 4 | Selected ranges of model parameters and numerical results for the synthetic multimodal anomaly example.

Model parameter	Range selected	Result
Anomaly 1		
K (nT.m^2)	1,000–20,000	5422.422
α (^{0})	-90—90	27.910
z (m)	1–300	14.817
x_0(m)	-3—3	29.387
q	0—3	1.964
Anomaly 2		
K (nT.m)	0—200	74.449
α (^{0})	–90—90	–14.445
z (m)	1–20	120.055
x_0(m)	–3—3	8.999
q	0—3	1.017
Elapsed time	55s	

Genetic Algorithm

GA is a search heuristic inspired by the theory of natural evolution. The algorithm reflects the process of natural selection where the fittest individuals are selected to reproduce for the next generation. A generational GA is initialized by a randomly generated population (set containing probable solutions), then the fitness (the objective function) of each individual is evaluated. Then, a new population is generated from the original one; this is aided by some GA operators: selection, crossover, and mutation. To form this new population, two solutions from the original population are selected considering their fitness. They are crossed over with the crossover probability to generate two new offspring who are then mutated with a mutation probability. The mutation guides against local minima. After obtaining the new generation, the steps are repeated. The algorithm terminates after reaching a finite number of generations; and the individual with the best fitness value returned as the solution to the problem. For this study, a crossover probability of 0.7 and a mutation probability of 0.1 was used for producing 800 generations.

TABLE 5 | Parameter results from inversion of sphere model anomaly using MRF, PSO, SA and GA techniques.

	True	MRF	PSO	SA	GA
K (nT.m^3)	11000.000	11001.300	11035.231	11374.306	10585.321
α (^{0})	60.000	60.000	59.783	61.621	61.218
z (m)	11.000	11.000	11.032	10.532	10.824
x_0 (m)	0.000	0.000	0.000	−0.010	0.007
q	2.500	2.500	2.498	2.552	2.531
RMS	—	3.22×10^{-5}	1.05×10^{-3}	5.85×10^{-2}	7.23×10^{-2}
Elapsed Time	—	30s	27s	22s	41s

Procedures consistent with PSO, SA, and GA were concurrently implemented on the synthetic sphere model constructed in *Synthetic Examples* Section. More also, bounds consistent with those used for MRF optimization were adopted. The results obtained are shown in **Table 5**. From the table, it can be observed that with an RMS of 3.22×10^{-5}, MRF optimization technique produced results of greater quality than its comparative counterparts. **Figure 8** shows the convergence character for the four techniques after 800 iterations. From the plots, it is observed that while all the methods achieved minimum errors in less than 250 iterations, MRF clearly boasted the fastest convergence. This advantage is accrued to the somersault foraging behavior of the procedure (as earlier explained in *Manta Ray Foraging Optimization Algorithm* Section). Notably, SA and GA did not achieve convergence even after 800 iterations. More too, from **Figure 9**, the MRF presented the greater error variability compared to GA, SA, and PSO. The superior interquartile curve indicates that the MRF algorithm possesses greater exploration capabilities than GA, SA, and PSO. This is expected as the MRF optimization algorithm allows for intelligent/situational switching between cyclone and chain foraging strategies. The chain foraging strategy favors local search while the cyclone foraging technique allows for extensive global exploration.

Case Studies

The performance of the new technique is further investigated using three field cases.

The Pima Copper Mine Anomaly

The Pima mine is an open pit, "complex" porphyry copper deposit located off the northeast flanks of the Sierrita Mountains at about 30 km south of Arizona, United States. At full production, the mine can produce up to 50,000 tons of copper per day (Hamel, 1979; Cox et al., 2006; Biswas et al., 2017).

Stratigraphically, the mine is fixated in an east-north-eastly striking and south-eastly dipping Paleozoic to Mesozoic sedimentary sequence intermediately intruded by quartz monzonite porphyry believed to be of Tertiary age (Abbas & Fedi, 2013). These Paleozoic sediments notably observed to be dolomites, limestones, and sandstones have historically been anti-frigidly metamorphized into calco-silicate skarns, marble, and quartzite and then, unconformably overlain by marginally recrystallized and hydrothermally altered Mesozoic to Triassic clastic (Cox et al., 2006). The intrusions have characteristically resulted in mineralization of high grade in the Paleozoic rocks and ore dissemination in the relatively younger Mesozoic sediments. Structurally, the area is dominated by east-west post-mineralization faults in the western part of the mine, and

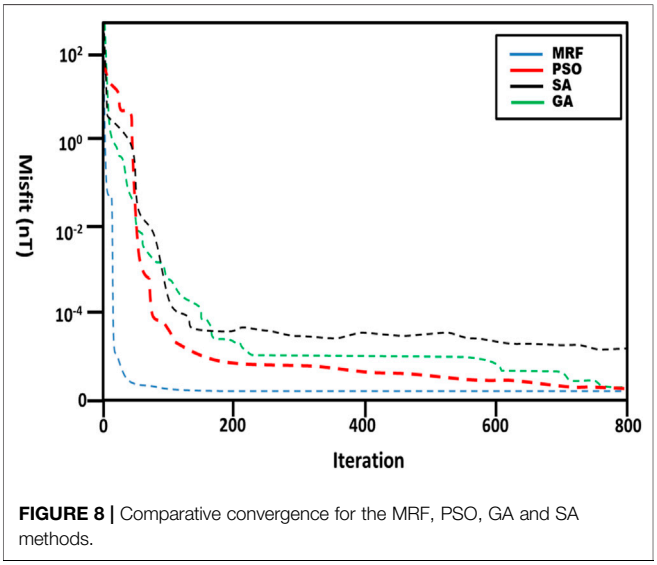

FIGURE 8 | Comparative convergence for the MRF, PSO, GA and SA methods.

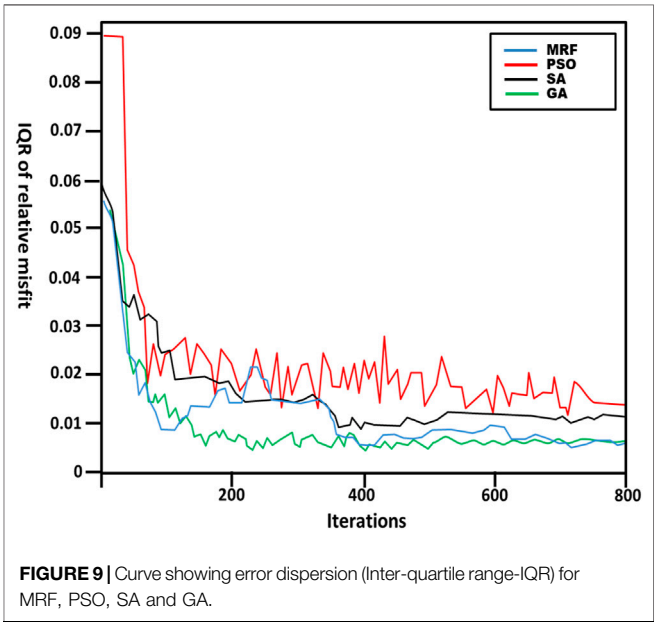

FIGURE 9 | Curve showing error dispersion (Inter-quartile range-IQR) for MRF, PSO, SA and GA.

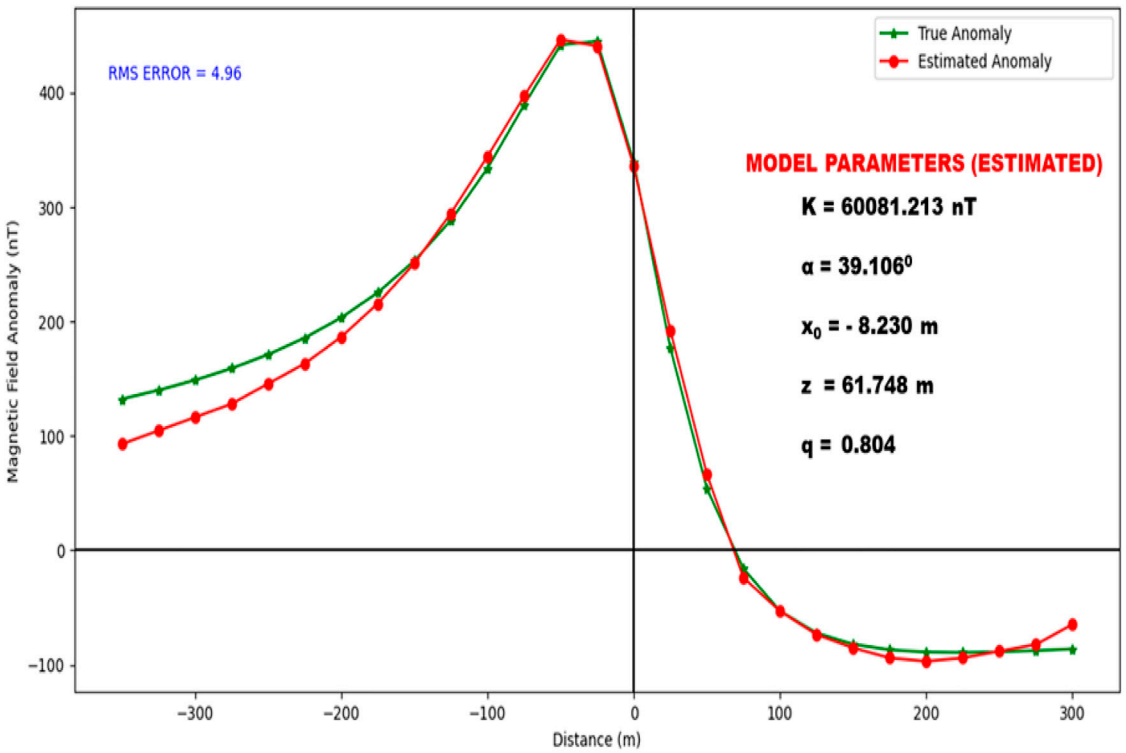

FIGURE 10 | Magnetic anomaly profile over the Pima copper mine anomaly, Arizona using the MRF algorithm.

TABLE 6 | Numerical results for Pima copper mine Anomaly.

Model parameters	Selected ranges	Result	Error	Time elapsed (s)
K (nT.m)	1,000–20,000	60081.313	4.96	33
α (^{0})	−90—90	39.106		
z (m)	0–500	61.748		
x_0(m)	−12–12	−8.230		
q	0–3	0.804		

strong shearing and faulting of low angle truncating the ore body at depth (Hamel, 1979; Barter & Kelly, 1982; Abbas & Fedi, 2013).

Figure 10 (red line with round markers) is a magnetic anomaly profile over a buried ore body retrieved from magnetic survey data taken across the Pima mine (Gay, 1963). The profile was digitized with a sampling interval of 25 m. In this research, the new method attempts at deciphering the parameters characterizing the geologic feature whose structure (initially unknown) can take any of the three studied geometric shapes. We initialize the algorithm using bounds indicated in **Table 6**. The algorithm is set to terminate after 1,000 iterations. At the end of the MRF optimization session, the misfit was monitored using the RMSE technique (**Figure 10**). The results obtained are displayed in **Table 6**.

TABLE 7 | Comparative analysis of parameter results for the Pima copper mine anomaly.

Model parameters	Gay (1963)	Venkata Raju (2003)	Abdelrahman et al. (2003b)	Tarantola (2005)	Mehanee et al. (2021)	Drilling information	Present study
K (nT.m)	—	—	80,550	39190.00	46,424.38	—	60081.31
α (^{0})	−50.00	−51.00	—	−44.70	−55.11	—	39.11
z (m)	70.00	76.81	68.00	64.10	71.00	64	61.75
x_0 (m)	—	—	—	—	—	—	−8.23
q	1.00	—	—	1.0	1.00	—	0.80

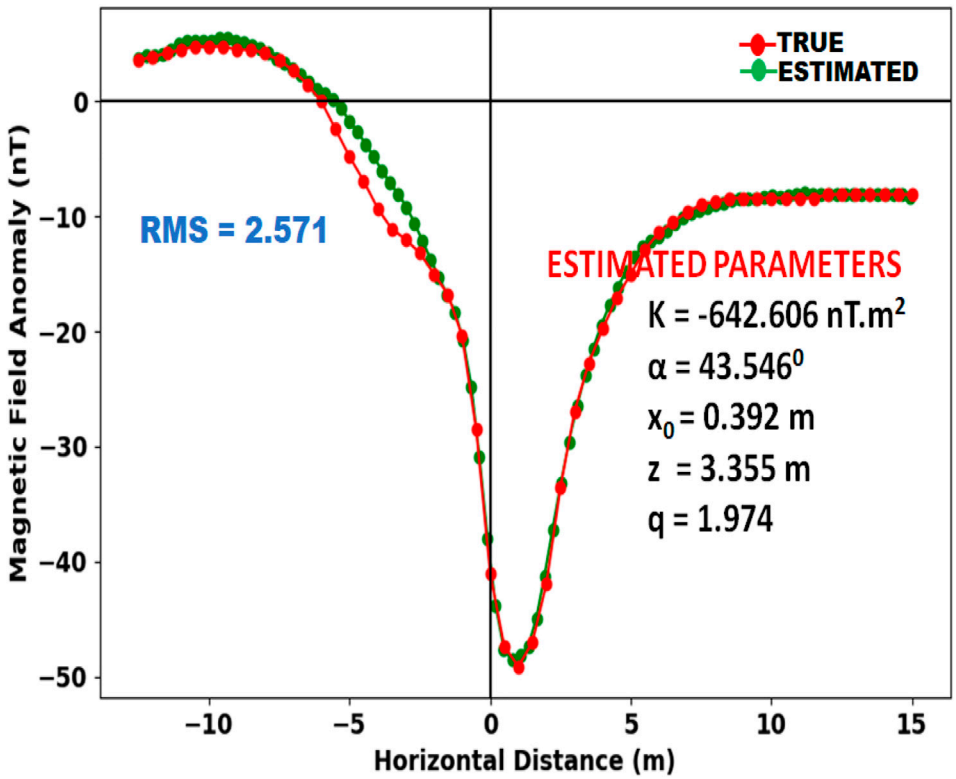

FIGURE 11 | Magnetic anomaly profile over the Parniaba field anomaly using the MRF algorithm.

TABLE 8 | Numerical results for the Parnaiba anomaly.

Model parameters	Selected ranges	Result	Error	Time elapsed (s)
K (nT.m^2)	–5,000–5,000	642.606	2.571	34
α (^{0})	–90–90	43.546		
z (m)	0–200	3.35		
x_0 (m)	–10–10	0.39		
q	0–3	1.97		

Results from analysis suggest that the investigated structure's shape compares appositely with that of a perfect thin sheet model. The parameters characterizing the model are estimated as K = 6,081.213 nT m, α = 39.106, x_o = -8.230 m and z = 61.748 m. More also, the obtained RMSE of 2.14 indicates that the actual and estimated data fits excellently.

We now attempt to compare these results with those from similar studies. Notably, the Pima anomaly has been widely interpreted in literature. Initially Gay (1963) used classical curve matching techniques to interpret the buried geologic feature as a sheet-like structure inclined at about -50° at a depth of 21.34 m. Venkata Raju, 2003) employed a LIMAT

TABLE 9 | Comparative analysis of parameter results for the Parnaiba anomaly.

Model parameters	Silva (1989)	Abdelrahman et al. (2019)	Abdelrahman et al. (2003a)	Tlas and Asfalhani (2011)	Tlas and Asfalhani (2015)	Present study
K (nT.m^2)	—	–717.90	–215.60	–552.30	–4007.6	642.606
α (^{0})	—	33.30	52.58	46.83	41.3	43.546
z (m)	3.50	3.50	2.23	3.36	3.4	3.35
x_0 (m)	—	—	—	—	—	0.39
q	—	—	—	2.00	2.00	1.97

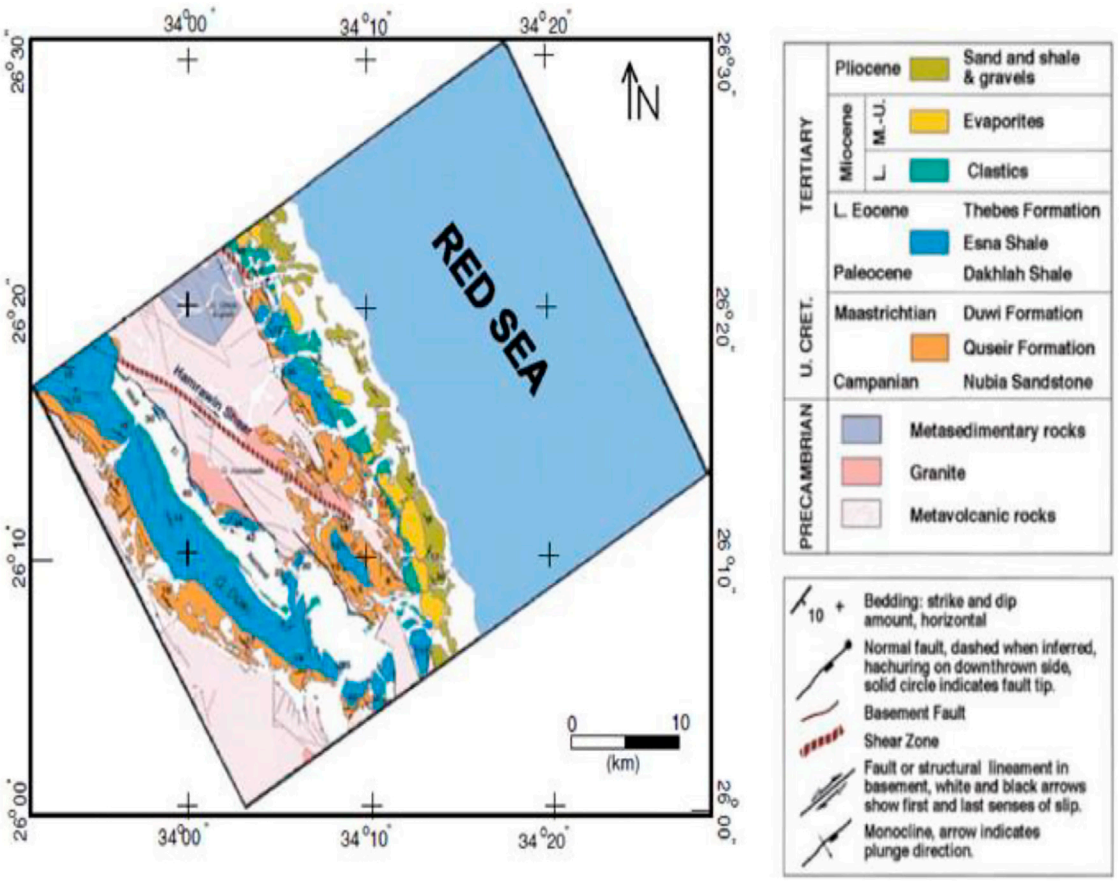

FIGURE 12 | Geologic map of the Quseir area, Egypt showing the Hamrawein shear (modified after Essa and Elhussein, 2018).

computer program for least-squares magnetic inversion over the Pima anomaly. After adequate smoothening of the initial solution using Marquarst's algorithm, he interpreted the anomaly as a thin sheet of depth -76.81 m. Recently, the buried anomaly was interpreted as between a thin sheet and dyke like structure using the simplex algorithm (Tlas & Asfahani, 2015). After calculations, Tlas & Asfahani (2015) gave the depth of the Pima copper anomaly as 64.1 m. Mehanee et al., 2021) employed an R-Parameter imaging method to pin-point the anomaly to a sheet-like structure buried at depth of 71 m. Petrophysical information reports the drilling depth as 64 m (Biswas, 2018). Considering these findings (**Table 7**), it can be concluded that results from our new methodology comparably agree acceptably with previous studies.

The Parnaiba Anomaly

In our second field case, we analyze crustal anomaly in the Parnaiba basin.

The Parnaíba basin is a 500,000 km-square wide Paleozoic basin structurally situated between the São Francisco and Amazonian cratons (Cordani et al., 2013; Daly et al., 2018) in north-east Brazil and widely regarded by explorationists as one of the world's most promising modern onshore gas basin. Priori regional studies report that the basin which is characterized by Neoproterozoic structures mapped to the Brazilian Orogenic Cycle (Mckenzie & Tribaldos, 2018) is accrued with 3–5 km of sediments in the main depo-center of its Phanerozoic-aged sedimentary rocks (Solon et al., 2018). These rocks overlie the Neoproterozoic structures of the Brazilian Orogenic Cycle. Oregenically, the crustal masses of this basin are convicted to be resultant from the massive splitting of the Rodinia believed to have occurred before the development of the trending Brazilian fold belts around 900 Ma (Cioccari & Mizusaki, 2019; Jurandyr Luciano Sanches Ross, 2020). Basement inliers were then formed with the surrounding of these classical cratonic fragments by Neoproterozoic fold belts during the amalgamation process of the Gondwana supercontinent. These inliers were further reworked thermally and contracted into cratonic nuclei during the Brazilian orogeny. However, the inclusive geo-magmatism widely observed in greater portions of the Parnaíba Basin has been associated with events of distention events and faults remobilization that followed the rupturing of the Pangea and the opening of the Atlantic Ocean (Cioccari & Mizusaki, 2019). Macedo Filho et al., 2019) reports that these magmatic occurrences in the basin as well as their associated geothermal gradients may have generated the much-acclaimed hydrocarbons in the sedimentary sequences of the Parnaíba Basin.

Figure 11 (red line with round markers) shows the vertical magnetic anomaly resulted from a 26 m-long profile over a

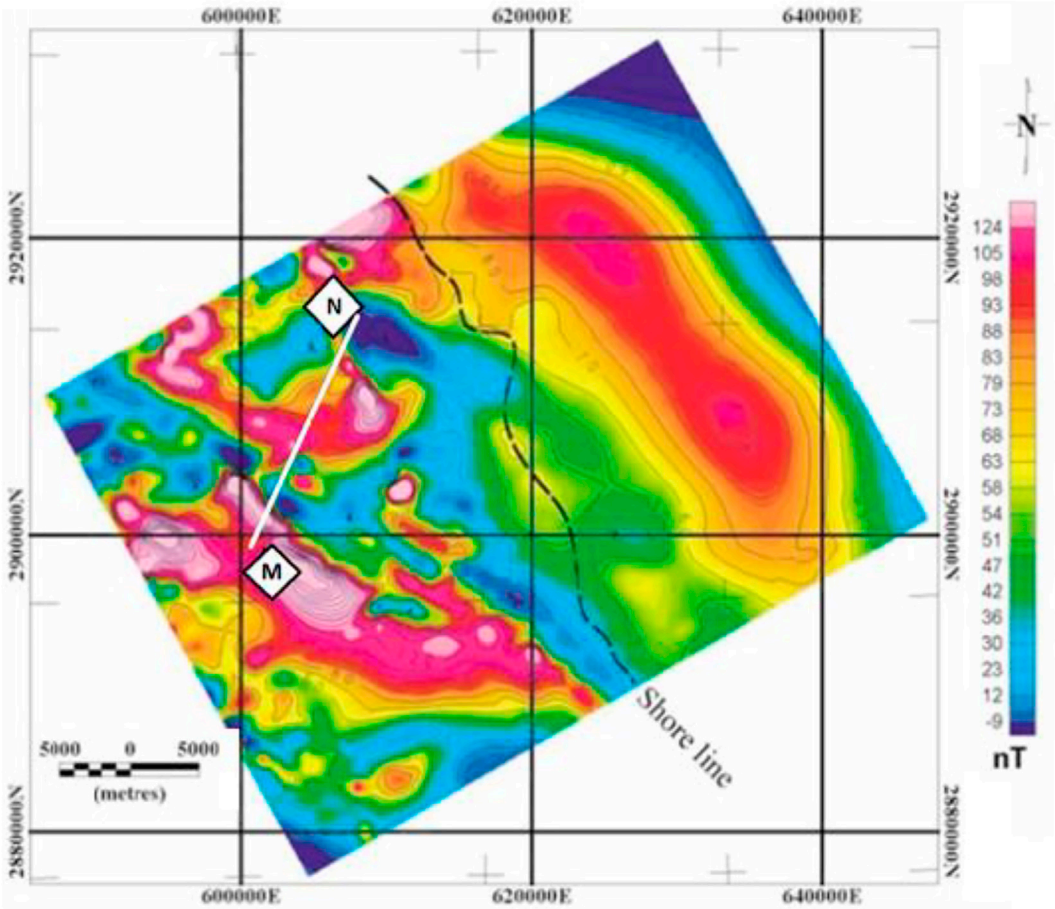

FIGURE 13 | Magnetic intensity map of the Hamrawein field area showing Profile MN (redrawn after Essa and Elhussein, 2018).

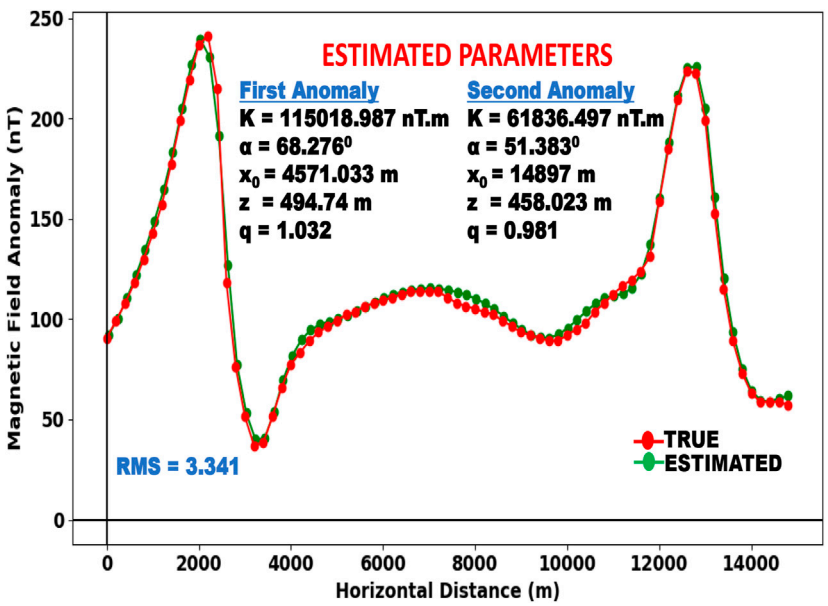

FIGURE 14 | Magnetic anomaly profile over the Hamrawein field anomaly using the MRF algorithm.

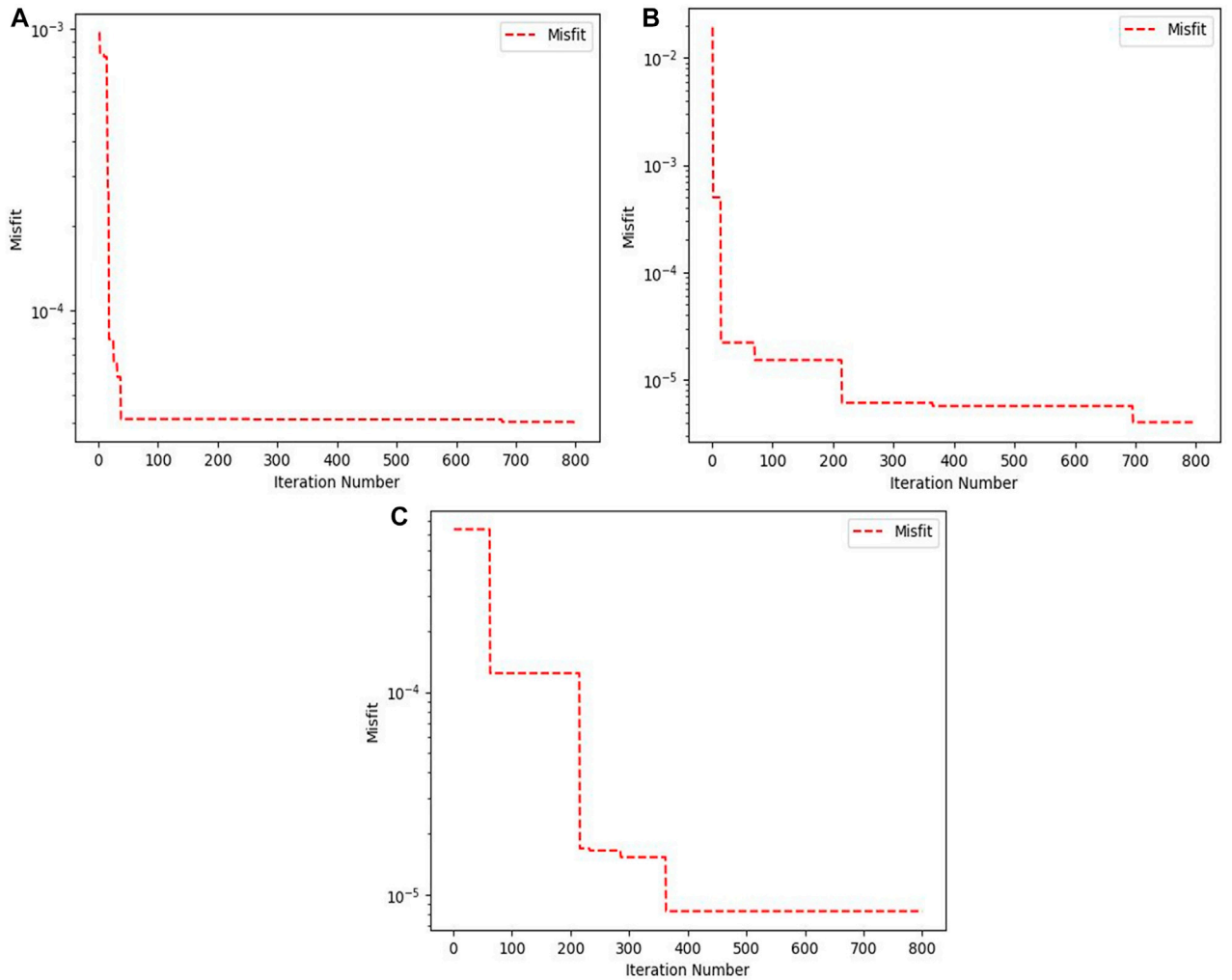

FIGURE 15 | Convergence behavior of the investigated case studies **(A)** Pima anomaly, **(B)** Parnaiba anomaly and **(C)** Hamrawein anomaly.

Mesozoic diabase intruded into the Paleozoic sediment of the Parnaiba basin. The profile was sampled at an interval of 0.5 m. The uniqueness of this anomaly problem lies in the fact that the oxidization of magnetite resultant from extensive weathering of the upper part of the buried structure has led to the loss of most of its magnetism (Silva, 1989). As a result of this geological peculiarity, we expect the magnetic anomaly to be largely affected by random noise at gross levels. This field case is also a test of the stability of the method in the presence of such peculiarity.

The anomaly depth, magnetic angle, amplitude coefficient, anomaly origin, and shape factor are estimated using MRF algorithm are guided by UB-LB outlined in **Table 8**. This magnetic anomaly is inverted with the cylinder model considered as the priori anomaly causative.

After each iterating round, the misfit between sample data and those from the estimated parameters are calculated (**Figure 11**). The obtained results are displayed in **Table 8**.

Comparatively, it can be observed that depth to the center of the anomaly estimated using our new method (z = 3.355 m) agrees with previous reports from similar studies by Silva (1989); Abdelrahman et al., 2019), Tlas and Asfahani, 2011), and Tlas and Asfahani, 2015). Silva (1989) obtained a depth of 3.5 m after converting the problem from non-linear to linear using the M-fitting technique; Abdelrahman et al., 2019 using the least square minimization method reported that the cylinder is buried at a depth of 3.5 m. On the other hand, Tlas & Asfahani (2011) and Tlas & Asfahani (2015) estimated the depth to the center of the cylinder as 3.36 and 3.4 m by respectively employing the deconvolution technique and simplex algorithm. Furthermore, the obtained values of K and RMSE confirm the algorithm's stability in the presence of contamination.

The results obtained using the present technique as well as those reported from the previous studies are displayed in **Table 9**.

The Hamrawein Field Anomaly

In our final case study, we will be analyzing a multi-model anomaly from Hamrawein field–an Egyptian mining field situated around the western throat of the Red Sea in North Africa. This geologic region is

TABLE 10 | Numerical Results for the Hamrawein field anomaly.

Model parameters	Selected ranges	Result
First Anomaly		
K (nT.m)	100–500,000	110531.368
α (^{0})	−90—90	65.031
z (m)	100–1,000	446.832
x_o (m)	0–15,000	2377.424
q	0–3	0.921
Second Anomaly		
K (nT.m)	100–500,000	49713.438
α (^{0})	−90—90	57.382
z (m)	100–1,000	399.963
x_o (m)	0–15,000	13629.462
q	0–3	0.873
Elapsed time	90s	

a constituted part of the East-African rift system believed to have been structurally architected from the anti-clockwise rotational divergence of the Arabian plate from the African tectonic Plate with the central Mediterranean Sea as the pole of rotation (Noweir & Fheel, 2015). The field is petrologically dominated with volcanic rocks such as pillow tholeiitic basalts overly genetically on layers of ultramafic and gabbroic strata. These layers of strata are unevenly covered with volcanic and sedimentary rocks of calco-alkaline geochemistry (Salem et al., 2005; Smith & Salem, 2005). **Figure 12** is a geological map of Qusier area showing the Hamrawein field.

Figures 13, **14** show a 15 km magnetic anomaly profile (MN) extracted from a magnetic map designed from an extensive high definition aeromagnetic survey data originally carried out by Salem et al. (1999). For this study, the profile is digitized at a 200 m interval. From priori geologic studies, we can ascertain that the profile is characterized by two prominent anomalies. However, the structure or characteristics of these anomalies cannot be distinctly defined initially and as such could be interpreted broadways as a combination of any of the simple shapes. This situation normally renders inherent non-uniqueness around solutions for the anomaly.

Fudging in the peculiarity of this problem and to resolve this technical complication, we run the algorithm for all possible dual-combinable shapes. The least RMSE error of 3.341 is achieved and accepted for model shapes with q values of 1.032 and 0.981 respectively which proximate synonymously with models of thin sheet structure. Then too, our algorithm eliminants K = 115,018.987 nT m, z = 494.74 m, α = 68.276° and x_o = 4571.033 m as optimal model parameters for the first buried structure while the parameters of the second structure are computed to be K = 61,836.497 nT m, z = 458.023 m, α = 51.383° and x_o = 14897 m (**Table 10**). From **Figure 14**, it can be observed that the fit between the observed and estimated anomalies is consistently excellent.

Table 11 compares results obtained in this present study with those obtained from similar studies reported in literature. Salem et al., 2005) modified the enhanced local wavenumber method and used it to interpret the two subsurface anomalies as thin sheet structures buried at depths of 555.7 and 441.2 m respectively. Salem et al., 2005) did heterological computation of the anomaly using analytic signal derivative but reported depths of 540 and 447 m respectively. Salem (2011) on the other hand conducted his analysis of the Hamrawein anomaly using both total gradient (TG) and local wave number (LW) methods. The LG methodology outputted depths of 486.5 and 440.4 m while the LW method out-turned 432.6 and 422.8 m as respective depths to the two anomalies. Essa & Elhussein, 2018 and Essa & Elhussein (2020) used particle swarm optimization (PSO) to carry out magnetic inversion for the area. While the former employed robust PSO for this task and reported the subsurface structures as thin sheets with depths of 623.05 and 494.14 m, the latter who emphasized the use of the optimization technique to infer second moving average residual magnetic anomalies also interpreted the structures as thin sheets but emplaced them at depths of 604 and 500 m respectively. Comparing results from this study with these previous findings, it can be generally deduced that resolutions using this new methodology stand in good agreement with those from previous reports. **Figure 15** shows the convergence behavior of the investigated case studies (Pima, Parnaiba, and Hamrawein anomalies).

Evaluation of results obtained using this new methodology has revealed that the technique exhibits admirable stability in the presence of noise, remarkable flexibility especially when confronted with interfering anomalies, and great pervasiveness in the quantitative resolution of magnetic inversion problems. The consistency of the results obtained from the analysis of the field

TABLE 11 | Comparative analysis of results for the Hamrawein field anomaly.

Model parameters	Salem et al. (2005)	Salem et al. (2005)	Salem (2011)	Essa & Elhussein (2018)	Mehanee et al. (2021)	Present study
First Anomaly						
K (nT.m)	—	—	127595.3	507.64	102046.00	115.02
α (^{0})	—	—	—	57.04	70.49	68.27
z (m)	555.7 ± 10	540 ± 30	486.5	623.05	480.00	494.74
x_o(m)	4526.00 ± 7	4530 ± 10	—	4255.98	4550.00	4571.03
q	1.44	-	1.0	0.89	1.00	1.03
Second anomaly						
K (nT.m)	—	—	83746.7	427.38	56549.52	61836.497
α (^{0})	—	—	—	37.21	55.04	51.383
z (m)	441.2 ± 3	477 ± 25	440.4	494.14	400.00	458.023
x_o (m)	14858.00 ± 17	14850 ± 21	—	14823.96	15200.00	148973.295
q	1.20	1.2 ± 01	1.0	0.93	1.00	0.981

examples when compared with background results from other similar studies conducted with other methods further affirms the reliability of the new methodology. While this consistency is continuous for shape and depth parameters, **Tables 6**, **8**, **10** show that there are significant variations in the amplitude parameter for all field cases. This large variation could be attributed to two main reasons. The first, which is the mathematical role of K in the forward model (**Equation 1**) has already been explained in *Synthetic Examples* Section. Ambiguity makes up the second reason. The K parameter—directly related to the magnetic susceptibility is a physical property that points to the type of materials making up the buried anomaly. As has been explained severally in literature (Clark, 1996; Crowther, 2003; Marques et al., 2014; Teixeira et al., 2018; César de Mello et al., 2020), magnetic susceptibility is a very non-unique rock property and could sometimes range up to factors of 10^4. It is therefore not surprising to find authors reporting different values for K. Howasmuch, it will be rather skewed to conduct appraisal of this parameter based on these literature reports alone. The efficiency of the new method in the estimation of K would only be assessed without bias if the result were gauged against laboratory findings for cores harvested from these field sites. Unfortunately, this information is not available for any of the three field cases. Nonetheless, the new technique still exhibited comparative edge over other well-known and conventional techniques especially on the grounds of convergence rate, and quality of the anomaly parameters (depth and shape) resolved.

CONCLUSION

In this study, we have introduced and investigated the applicability and the performance of the Manta Ray Foraging Optimization algorithm in elucidating distinctive physical parameters of simple geometrically shaped geologic structures (spheres, horizontal cylinders, and thin sheets). This new inversion technique has been demonstrated successfully on synthetically generated magnetic anomalies corrupted with different levels of Gaussian noise (0, 5, 10, 15, 20%), applied to cases of anomalies from multiple and intercalating structures, and finally experimented on heterologous field cases taken from mining sites in Brazil, United States, and Egypt.

Generally, the test examples (real and synthetic) treated in this research work have all affirmed the MRF-based algorithm's suitability for the inverse modeling of magnetic anomalies caused by conventional geometrically shaped structures. Furthermore, the examples enabled us in the evaluation of the new technique's strengths with regards to geophysical optimization and extendedly, as compared with existing methods. First, considering reports so far published and even that from the comparative study in this work, it has been observed that amongst stochastic geophysical optimization techniques, the proposed algorithm presents one of the best convergence rates. This rate, however, has no effect on its optimization abilities, as the misfits calculated at the culmination of the procedure still fell within acceptable levels. Most significantly, the method was able to address the reoccurring challenge of immature convergence and local optima (commonly resulting in poor solutions) encountered by conventional intelligent methods such as DE, PSO, GA, and ACO. This is enabled by the search agents' propensity to transition between chain and cyclone foraging strategies. The chain strategy contributes to the algorithm's local search ability, whereas the cyclone foraging behavior is significantly dedicated to the algorithm's global search capacity; a combination of these two, as permitted by our new method, enables extensive exploration of the entire problem domain and practically, greatly improved the quality of solutions. It should however be added that while the algorithm converge in fewer iterations, it took a longer time to complete an iteration. This is but a limitation of this method. As a recommendation, this temporal cost could be improved through modifications (e.g., binary-MRF, quantum-MRF, Chaotic-MRF) and hybridization (e.g., PSO-MRF, GA-MRF, ACO-MRF) of the technique. Considering these gains, and the significantly lower computational effort required to attain them (gauging the limitation), MRF has been proven to positively outperform conventional optimizers in the resolution of geophysical optimization problems with respect to geometrically shaped magnetic anomalies.

Hereto, the novel methodology can be recommended for ore/mineral exploration as well as reconnaissance studies aimed at efficiently resolving subsurface structures from magnetic field data. As a recommendation for future studies, the method can be further developed for the interpretation of other potential field data such as resistivity and self-potential data.

DATA AVAILABILITY STATEMENT

The original contributions presented in the study are included in the article/Supplementary Material, further inquiries can be directed to the corresponding author.

AUTHOR CONTRIBUTIONS

UB, SE, AA, and CM prepared data, applied methodology, writing the first draft of the manuscript. AE, KA, and DG-O revised the manuscript, methodology, and editing the manuscript.

FUNDING

We declare all sources of funding received for the research being submitted. Researchers Supporting Project number (RSP-2022/351), King Saud University, Riyadh, Saudi Arabia.

ACKNOWLEDGMENTS

Deep thanks and gratitude to the Researchers Supporting Project number (RSP-2022/351), King Saud University, Riyadh, Saudi Arabia for funding this research article. The authors wish to thank the management of the University of Calabar for providing the facilities used for this research.

REFERENCES

Abbas, M. A., and Fedi, M. (2013). "Automatic DEXP Imaging of Potential fields Independent of the Structural Index," in 75th European Association of Geoscientists and Engineers Conference and Exhibition 2013 Incorporating SPE EUROPEC 2013, European Association of Geoscientists & Engineers, London, United Kingdom. doi:10.3997/2214-4609.20130120

Abdelrahman, E.-S. M., Abo-Ezz, E. R., and Essa, K. S. (2012). Parametric Inversion of Residual Magnetic Anomalies Due to Simple Geometric Bodies. *Exploration Geophys.* 43, 178–189. doi:10.1071/EG11026

Abdelrahman, E.-S. M., El-Araby, H. M., El-Araby, Tarek., and Essa, Khalid. (2003a). A Numerical Approach to Depth Determination from Magnetic Data. *Kuwait J. Sci. Eng.* 29, 121–134.

Abdelrahman, E.-S. M., El-Araby, T. M., and Essa, K. S. (2003b). A Least-Squares Minimisation Approach to Depth, index Parameter, and Amplitude Coefficient Determination from Magnetic Anomalies Due to Thin Dykes. *Exploration Geophys.* 34, 241–248. doi:10.1071/eg03241

Abdelrahman, E. M., Abdelazeem, M., and Gobashy, M. (2019). A Minimization Approach to Depth and Shape Determination of Mineralized Zones from Potential Field Data Using the Nelder-Mead Simplex Algorithm. *Ore Geology. Rev.* 114, 103123. doi:10.1016/j.oregeorev.2019.103123

Abo-Ezz, E. R., and Essa, K. S. (2016). A Least-Squares Minimization Approach for Model Parameters Estimate by Using a New Magnetic Anomaly Formula. *Pure Appl. Geophys.* 173, 1265–1278. doi:10.1007/s00024-015-1168-9

Agarwal, A., Chandra, A., Shalivahan, S., and Singh, R. K. (2018). Grey Wolf Optimizer: a New Strategy to Invert Geophysical Data Sets. *Geophys. Prospecting* 66, 1215–1226. doi:10.1111/1365-2478.12640

Araffa, S. A. S., El-bohoty, M., Abou Heleika, M., Mekkawi, M., Ismail, E., Khalil, A., et al. (2018). Implementation of Magnetic and Gravity Methods to Delineate the Subsurface Structural Features of the Basement Complex in central Sinai Area, Egypt. *NRIAG J. Astron. Geophys.* 7, 162–174. doi:10.1016/j.nrjag.2017.12.002

Asfahani, J., and Tlas, M. (2012). Fair Function Minimization for Direct Interpretation of Residual Gravity Anomaly Profiles Due to Spheres and Cylinders. *Pure Appl. Geophys.* 169, 157–165. doi:10.1007/s00024-011-0319-x

Balkaya, Ç., Ekinci, Y. L., Göktürkler, G., and Turan, S. (2017). 3D Non-linear Inversion of Magnetic Anomalies Caused by Prismatic Bodies Using Differential Evolution Algorithm. *J. Appl. Geophys.* 136, 372–386. doi:10.1016/j.jappgeo.2016.10.040

Balkaya, Ç., and Kaftan, I. (2021). Inverse Modelling via Differential Search Algorithm for Interpreting Magnetic Anomalies Caused by 2D Dyke-Shaped Bodies. *J. Earth Syst. Sci.* 130. doi:10.1007/s12040-021-01614-1

Barter, C. F., and Kelly, J. L. (1982). *Geology of the Twin Buttes mineral deposit, Pima Mining District, Pima County, Arizona. Advances in Geology of the Porphyry Copper Deposits*. Tucson: University of Arizona Press, 407–432.

Ben, U. C., Akpan, A. E., Enyinyi, E. O., and Awak, E. (2021b). Novel Technique for the Interpretation of Gravity Anomalies over Geologic Structures with Idealized Geometries Using the Manta ray Foraging Optimization. *J. Asian Earth Sci. X* 6, 100070. doi:10.1016/j.jaesx.2021.100070

Ben, U. C., Akpan, A. E., Mbonu, C. C., and Ebong, E. D. (2021a). Novel Methodology for Interpretation of Magnetic Anomalies Due to Two-Dimensional Dipping Dikes Using the Manta Ray Foraging Optimization. *J. Appl. Geophys.* 192, 104405. doi:10.1016/j.jappgeo.2021.104405

Ben, U. C., Akpan, A. E., Mbonu, C. C., and Ufuafuonye, C. H. (2021c). Integrated Technical Analysis of Wind Speed Data for Wind Energy Potential Assessment in Parts of Southern and central Nigeria. *Clean. Eng. Technology* 2, 100049. doi:10.1016/j.clet.2021.100049

Biswas, A., and Acharya, T. (2016). A Very Fast Simulated Annealing Method for Inversion of Magnetic Anomaly over Semi-infinite Vertical Rod-type Structure. *Model. Earth Syst. Environ.* 2, 1–10. doi:10.1007/s40808-016-0256-x

Biswas, A. (2018). Inversion of Source Parameters from Magnetic Anomalies for Mineral/Ore Deposits Exploration Using Global Optimization Technique and Analysis of Uncertainty. *Nat. Resour. Res.* 27, 77–107. doi:10.1007/s11053-017-9339-2

Biswas, A., Mandal, A., Sharma, S. P., and Mohanty, W. K. (2014). Delineation of Subsurface Structures Using Self-Potential, Gravity, and Resistivity Surveys from South Purulia Shear Zone, India: Implication to Uranium Mineralization. *Interpretation* 2, T103–T110. doi:10.1190/INT-2013-0170.1

Biswas, A., Parija, M. P., and Kumar, S. (2017). Global Nonlinear Optimization for the Interpretation of Source Parameters from Total Gradient of Gravity and Magnetic Anomalies Caused by Thin Dyke. *Ann. Geophys.* doi:10.4401/ag-7129

César de Mello, D., Demattê, J. A. M., Silvero, N. E. Q., Di Raimo, L. A. D. L., Poppiel, R. R., Mello, F. A. O., et al. (2020). Soil Magnetic Susceptibility and its Relationship with Naturally Occurring Processes and Soil Attributes in Pedosphere, in a Tropical Environment. *Geoderma* 372, 114364. doi:10.1016/j.geoderma.2020.1143610.1016/j.geoderma.2020.114364

Cioccari, G. M., and Mizusaki, A. M. P. (2019). Sistemas Petrolíferos Atípicos Nas Bacias Paleozoicas Brasileiras - Uma Revisão. *Geociencias* 38, 367–390. doi:10.5016/geociencias.v38i2.13173

Clark, A. J. (1996). "Magnetic Susceptibility Survey," in *The Experimental Earthwork Project, 1960–1992. 118–121*. Editors M. G. Bell, P. J. Fowler, and S. W. Hilson (York: Council for British Archaeology Research Report).

Cordani, U. G., Pimentel, M. M., Araújo, C. E. G. d., and Fuck, R. A. (2013). The Significance of the -Transbrasiliano-Kandi Tectonic Corridor for the Amalgamation of West Gondwana. *Braz. J. Geol.* 43, 583–597. doi:10.5327/Z2317-48892013000300012

Cox, D. P., Force, E. R., Wilkinson, W. H., More, S. W., Rivera, J. S., and Wooden, J. L. (2006). *The Ajo Mining District, Pima County, Arizona-evidence for Middle Cenozoic Detachment Faulting, Plutonism, Volcanism, and Hydrothermal Alteration*. Reston, VA: U.S. Geological Survey. doi:10.3133/pp1733

Crowther, J. (2003). Potential Magnetic Susceptibility and Fractional Conversion Studies of Archaeological Soils and Sediments*. *Archaeometry* 45 (4), 685–701. doi:10.1046/j.1475-4754.2003.00137.x

Daly, M. C., Fuck, R. A., Julià, J., Macdonald, D. I. M., and Watts, A. B. (2018). Cratonic basin Formation: a Case Study of the Parnaíba Basin of Brazil. *Geol. Soc. Lond. Spec. Publications* 472, 1–15. doi:10.1144/SP472.20

Di Maio, R., Milano, L., and Piegari, E. (2020). Modeling of Magnetic Anomalies Generated by Simple Geological Structures through Genetic-Price Inversion Algorithm. *Phys. Earth Planet. Interiors* 305, 106520. doi:10.1016/j.pepi.2020.106520

Dondurur, D., and Pamukçu, O. A. (2003). Interpretation of Magnetic Anomalies from Dipping dike Model Using Inverse Solution, Power Spectrum and Hilbert Transform Methods. *J. Balkan Geophys. Soc.*

Du, W., Cheng, L., and Li, Y. (2021). Lp Norm Smooth Inversion of Magnetic Anomaly Based on Improved Adaptive Differential Evolution. *Appl. Sci.* 11, 1072. doi:10.3390/app11031072

Duong, T. Q. C., Dương, Đ. H., Phạm, N. N., Nguyễn, H. T., and Danh, A. (2021). Interpretation for Magnetic Data at Low Latitude Areas Using Continuous Wavelet Transform and Marquardt Algorithm. *Sci. Tech. Dev. J. - Nat. Sci.* 5, first. doi:10.32508/stdjns.v5i2.957

Ekinci, Y. L., Balkaya, Ç., Göktürkler, G., and Özyalın, Ş. (2020). Gravity Data Inversion for the Basement Relief Delineation through Global Optimization: A Case Study from the Aegean Graben System, Western Anatolia, Turkey. *Geophys. J. Int.* 224, 923–944. doi:10.1093/gji/ggaa492

Ekinci, Y. L., Balkaya, Ç., and Göktürkler, G. (2019). Parameter Estimations from Gravity and Magnetic Anomalies Due to Deep-Seated Faults: Differential Evolution versus Particle Swarm Optimization. *Turkish J. Earth Sci.* doi:10.3906/yer-1905-3

Elaziz, M. A., Hosny, K. M., Salah, A., Darwish, M. M., Lu, S., Sahlol, A. T., et al. (2020). New Machine Learning Method for Image-Based Diagnosis of COVID-19. *PLoS ONE* 15, e0235187. doi:10.1371/journal.pone.0235187

Essa, K. S., and Elhussein, M. (2020). Interpretation of Magnetic Data Through Particle Swarm Optimization: Mineral Exploration Cases Studies. *Nat. Resour. Res.* 29, 521–537. doi:10.1007/s11053-020-09617-3

Essa, K. S., and Elhussein, M. (2018). PSO (Particle Swarm Optimization) for Interpretation of Magnetic Anomalies Caused by Simple Geometrical Structures. *Pure Appl. Geophys.* 175, 3539–3553. doi:10.1007/s00024-018-1867-0

Essa, K. S., Mehanee, S. A., Soliman, K. S., and Diab, Z. E. (2020). Gravity Profile Interpretation Using the R-Parameter Imaging Technique with Application to Ore Exploration. *Ore Geology. Rev.* 126, 103695. doi:10.1016/j.oregeorev.2020.103695

Essa, K. S., Mehanee, S., and Elhussein, M. (2021). Magnetic Data Profiles Interpretation for Mineralized Buried Structures Identification Applying the

Variance Analysis Method. *Pure Appl. Geophys.* 178, 973–993. doi:10.1007/s00024-020-02553-6

Gay, S. P. (1963). Standard Curves for Interpretation of Magnetic Anomalies over Long Tabular Bodies. *Geophysics* 28, 161–200. doi:10.1190/1.1439164

Gay, S. P. (1965). Standard Curves for Magnetic Anomalies over Long Horizontal Cylinders. *Geophysics* 30, 818–828. doi:10.1190/1.1439656

Gharehchopogh, F. S., and Gholizadeh, H. (2019). A Comprehensive Survey: Whale Optimization Algorithm and its Applications. *Swarm Evol. Comput.* 48, 1–24. doi:10.1016/j.swevo.2019.03.004

Ghosh, K. K., Guha, R., Bera, S. K., Kumar, N., and Sarkar, R. (2021). S-shaped versus V-Shaped Transfer Functions for Binary Manta ray Foraging Optimization in Feature Selection Problem. *Neural Comput. Applic.* doi:10.1007/s00521-020-05560-9

Gobashy, M., Abdelazeem, M., and Abdrabou, M. (2020). Minerals and Ore Deposits Exploration Using Meta-Heuristic Based Optimization on Magnetic Data. *Contrib. Geophys. Geod.* 50, 161–199. doi:10.31577/congeo.2020.50.2.1

Gupta, S., and Deep, K. (2019). A Novel Random Walk Grey Wolf Optimizer. *Swarm Evol. Comput.* 44, 101–112. doi:10.1016/j.swevo.2018.01.001

Hamel, J. V. (1979). "Pima Mine Slope Failure, Arizona, U.S.A," in *Developments in Geotechnical Engineering*, 633–649. doi:10.1016/B978-0-444-41508-0.50026-0

Hassan, M. H., Houssein, E. H., Mahdy, M. A., and Kamel, S. (2021). An Improved Manta ray Foraging Optimizer for Cost-Effective Emission Dispatch Problems. *Eng. Appl. Artif. Intelligence* 100, 104155. doi:10.1016/j.engappai.2021.104155

Hayyolalam, V., and Pourhaji Kazem, A. A. (2020). Black Widow Optimization Algorithm: A Novel Meta-Heuristic Approach for Solving Engineering Optimization Problems. *Eng. Appl. Artif. Intelligence* 87, 103249. doi:10.1016/j.engappai.2019.103249

Hemeida, M. G., Alkhalaf, S., Mohamed, A.-A. A., Ibrahim, A. A., and Senjyu, T. (2020). Distributed Generators Optimization Based on Multi-Objective Functions Using Manta Rays Foraging Optimization Algorithm (MRFO). *Energies* 13, 3847. doi:10.3390/en13153847

Houssein, E. H., Emam, M. M., and Ali, A. A. (2021). Improved Manta ray Foraging Optimization for Multi-Level Thresholding Using COVID-19 CT Images. *Neural Comput. Applic* 33, 16899–16919. doi:10.1007/s00521-021-06273-3

Jurandyr Luciano Sanches Ross (2020). *Brazilian Relief, Planation Surfaces and Morphological Levels*. William Morris Davis – Revista de Geomorfologia. doi:10.48025/issn2675-6900.v1n1.p264-285.2020

Kennedy, J., and Eberhart, R. (1995). "Particle Swarm Optimization," in IEEE International Conference on Neural Networks - Conference Proceedings. doi:10.4018/ijmfmp.2015010104

Kirkpatrick, S., Gelatt, C. D., and Vecchi, M. P. (1983). Optimization by Simulated Annealing. *Science* 220, 671–680. doi:10.1126/science.220.4598.671

Klein, C. E., Segundo, E. H. V., Mariani, V. C., and dos S. Coelho, L. (2016). Modified Social-Spider Optimization Algorithm Applied to Electromagnetic Optimization. *IEEE Trans. Magn.* 52, 1–4. doi:10.1109/TMAG.2015.2483059

Kombe, E. Y., and Muguthu, J. (2019). Wind Energy Potential Assessment of Great Cumbrae Island Using Weibull Distribution Function. *Jenrr*, 1–8. doi:10.9734/jenrr/2019/v2i229734

Liu, S., Hu, X., Liu, T., Xi, Y., Cai, J., and Zhang, H. (2015). Ant colony Optimisation Inversion of Surface and Borehole Magnetic Data under Lithological Constraints. *J. Appl. Geophys.* 112, 115–128. doi:10.1016/j.jappgeo.2014.11.010

Macêdo Filho, A. A., Archanjo, C. J., Hollanda, M. H. B. M., and Negri, F. A. (2019). Mineral Chemistry and crystal Size Distributions of Mafic Dikes and Sills on the Eastern Border of the Parnaíba Basin, NE Brazil. *J. Volcanology Geothermal Res.* 337, 69–80. doi:10.1016/j.jvolgeores.2019.03.021

Marques, J., Siqueira, D. S., Camargo, L. A., Teixeira, D. D. B., Barrón, V., and Torrent, J. (2014). Magnetic Susceptibility and Diffuse Reflectance Spectroscopy to Characterize the Spatial Variability of Soil Properties in a Brazilian Haplustalf. *Geoderma* 219-220, 63–71. doi:10.1016/j.geoderma.2013.12.007

Mbonu, C. C., and Ben, U. C. (2021). *Assessment of Radiation hazard Indices Due to Natural Radioactivity in Soil Samples from Orlu*. Imo State, Nigeria: Heliyon. doi:10.1016/j.heliyon.2021.e07812

Mbonu, C. C., Essiett, A., and Ben, U. C. (2021). Geospatial Assessment of Radiation hazard Indices in Soil Samples from Njaba, Imo State, South-Eastern Nigeria. *Environ. Challenges* 4, 100117. doi:10.1016/j.envc.2021.100117

Mckenzie, D., and Rodríguez Tribaldos, V. (2018). Lithospheric Heating by Crustal Thickening: a Possible Origin of the Parnaíba Basin. *Geol. Soc. Lond. Spec. Publications* 472, 37–44. doi:10.1144/SP472.5

Mehanee, S. A. (2022b). A New Scheme for Gravity Data Interpretation by a Faulted 2-D Horizontal Thin Block: Theory, Numerical Examples and Real Data Investigation. *IEEE Trans. Geosci. Remote Sensing*, 1. doi:10.1109/TGRS.2022.3142628

Mehanee, S. A. (2014). An Efficient Regularized Inversion Approach for Self-Potential Data Interpretation of Ore Exploration Using a Mix of Logarithmic and Non-logarithmic Model Parameters. *Ore Geology. Rev.* 57, 87–115. doi:10.1016/j.oregeorev.2013.09.002

Mehanee, S. A. (2022a). Simultaneous Joint Inversion of Gravity and Self-Potential Data Measured along Profile: Theory, Numerical Examples, and a Case Study from Mineral Exploration with Cross Validation from Electromagnetic Data. *IEEE Trans. Geosci. Remote Sensing* 60, 1–20. doi:10.1109/TGRS.2021.3071973

Mehanee, S., Essa, K. S., and Diab, Z. E. (2021). Magnetic Data Interpretation Using a New R-Parameter Imaging Method with Application to mineral Exploration. *Nat. Resour. Res.* 30, 77–95. doi:10.1007/s11053-020-09690-8

Mehanee, S., Golubev, N., and Zhdanov, M. S. (1998). Weighted Regularized Inversion of Magnetotelluric Data. *SEG Annu. Meet.* 1998. doi:10.1190/1.1820468

Mehanee, S., and Zhdanov, M. (2004). A Quasi-Analytical Boundary Condition for Three-Dimensional Finite Difference Electromagnetic Modeling. *Radio Sci.* 39 (6), a–n. doi:10.1029/2004RS003029

Noweir, M. A., and Fheel*, A. S. (2015). *Structural Evolution of Extensional Phanerozoic Rift Blocks: El Hamrawein Area, Northwest Red Sea, Eastern Desert*. Egypt. doi:10.1190/ice2015-2212373

Ouadfel, S., and Taleb-Ahmed, A. (2016). Social Spiders Optimization and Flower Pollination Algorithm for Multilevel Image Thresholding: A Performance Study. *Expert Syst. Appl.* 55, 566–584. doi:10.1016/j.eswa.2016.02.024

Ouyang, F., and Chen, L. (2020). Iterative Magnetic Forward Modeling for High Susceptibility Based on Integral Equation and Gauss-Fast Fourier Transform. *Geophysics* 85, J1–J13. doi:10.1190/geo2018-0851.1

Pan, J., Wang, X., Zhang, X., Xu, Z., Zhao, P., Tian, X., et al. (2009). 2D Multi-Scale Hybrid Optimization Method for Geophysical Inversion and its Application. *Appl. Geophys.* 6, 337–348. doi:10.1007/s11770-009-0034-x

Pellerin, L., and Wannamaker, P. E. (2005). Multi-dimensional Electromagnetic Modeling and Inversion with Application to Near-Surface Earth Investigations. *Comput. Electronics Agric.* 46, 71–102. doi:10.1016/j.compag.2004.11.017

Portniaguine, O., and Zhdanov, M. S. (2000b). 3-D Magnetic Inversion with Data Compression and Image Focusing. *Geophysics* 67 (5), 1532–1541.

Portniaguine, O., and Zhdanov, M. S. (2000a). 3-D Magnetic Regularized Inversion with Data Compression and Image Focusing. *SEG Tech. Program Expanded Abstr.* doi:10.1190/1.1816073

Prakasa Rao, T. K. S., and Subrahmanyam, M. (1988). Characteristic Curves for the Inversion of Magnetic Anomalies of Spherical Ore Bodies. *Pure Appl. Geophys. PAGEOPH*. doi:10.1007/bf00876915

Rao, B. S. R., Radhakrishna Murthy, I. V., and Visweswara Rao, C. (1973). A Computer Program for Interpreting Vertical Magnetic Anomalies of Spheres and Horizontal Cylinders. *Pageoph* 110, 2056–2065. doi:10.1007/BF00876569

Salcedo-Sanz, S., Cornejo-Bueno, L., Prieto, L., Paredes, D., and García-Herrera, R. (2018). Feature Selection in Machine Learning Prediction Systems for Renewable Energy Applications. *Renew. Sustainable Energ. Rev.* 90, 728–741. doi:10.1016/j.rser.2018.04.008

Salem, A., Elsirafi, A., and Ushijima, K. (1999). *Design and Application of High-Resolution Aeromagnetic Survey over Gebel Duwi Area and its*

Offshore Extension. Egypt: Memoirs of the Graduate School of Engineering, Kyushu University.

Salem, A. (2011). Multi-deconvolution Analysis of Potential Field Data. *J. Appl. Geophys.* 74, 151–156. doi:10.1016/j.jappgeo.2011.04.001

Salem, A., Ravat, D., Smith, R., and Ushijima, K. (2005). Interpretation of Magnetic Data Using an Enhanced Local Wavenumber (ELW) Method. *Geophysics* 70, L7–L12. doi:10.1190/1.1884828

Silva, J. B. C. (1989). Transformation of Nonlinear two-dimensional Problems into Linear Ones Applied to the Magnetic Field of a Prism. *Geophysics* 54, 114–121. doi:10.1190/1.1442568

Smith, R. S., and Salem, A. (2005). Imaging Depth, Structure, and Susceptibility from Magnetic Data: The Advanced Source-Parameter Imaging Method. *Geophysics* 70, L31–L38. doi:10.1190/1.1990219

Solon, F. F., Fontes, S. L., and La Terra, E. F. (2018). Electrical Conductivity Structure across the Parnaíba Basin, NE Brazil. *Geol. Soc. Lond. Spec. Publications* 472, 109–126. doi:10.1144/SP472.19

Tarantola, A. (2005). "Inverse Problem Theory and Methods for Model Parameter Estimation," in *Inverse Problem Theory and Methods for Model Parameter Estimation*. doi:10.1137/1.9780898717921

Teixeira, D. D. B., Marques, J., Siqueira, D. S., Vasconcelos, V., Carvalho, O. A., Martins, É. S., et al. (2018). Mapping Units Based on Spatial Uncertainty of Magnetic Susceptibility and clay Content. *Catena* 164, 79–87. doi:10.1016/j.catena.2017.12.038

Tlas, M., and Asfahani, J. (2011). Fair Function Minimization for Interpretation of Magnetic Anomalies Due to Thin Dikes, Spheres and Faults. *J. Appl. Geophys.* 75, 237–243. doi:10.1016/j.jappgeo.2011.06.025

Tlas, M., and Asfahani, J. (2015). The Simplex Algorithm for Best-Estimate of Magnetic Parameters Related to Simple Geometric-Shaped Structures. *Math. Geosci.* 47, 301–316. doi:10.1007/s11004-014-9549-7

Venkata Raju, D. C. (2003). LIMAT: A Computer Program for Least-Squares Inversion of Magnetic Anomalies over Long Tabular Bodies. *Comput. Geosciences*. doi:10.1016/S0098-3004(02)00108-5

Wang, J.-S., and Li, S.-X. (2019). An Improved Grey Wolf Optimizer Based on Differential Evolution and Elimination Mechanism. *Sci. Rep.* 9. doi:10.1038/s41598-019-43546-3

Xie, W., Wang, Y.-C., Liu, X.-Q., Bi, C.-C., Zhang, F.-Q., Fang, Y., et al. (2019). Nonlinear Joint PP-PS AVO Inversion Based on Improved Bayesian Inference and LSSVM. *Appl. Geophys.* 16, 64–76. doi:10.1007/s11770-019-0750-9

Xu, H., Song, H., Xu, C., Wu, X., and Yousefi, N. (2020). Exergy Analysis and Optimization of a HT-PEMFC Using Developed Manta Ray Foraging Optimization Algorithm. *Int. J. Hydrogen Energ.* 45, 30932–30941. doi:10.1016/j.ijhydene.2020.08.053

Zhao, W., Zhang, Z., and Wang, L. (2020). Manta ray Foraging Optimization: An Effective Bio-Inspired Optimizer for Engineering Applications. *Eng. Appl. Artif. Intelligence* 87, 103300. doi:10.1016/j.engappai.2019.103300

Conflict of Interest: The authors declare that the research was conducted in the absence of any commercial or financial relationships that could be construed as a potential conflict of interest.

Publisher's Note: All claims expressed in this article are solely those of the authors and do not necessarily represent those of their affiliated organizations, or those of the publisher, the editors and the reviewers. Any product that may be evaluated in this article, or claim that may be made by its manufacturer, is not guaranteed or endorsed by the publisher.